

Active tectonic field for CO₂ Storage management: Hontomín onshore study-case (SPAIN)

Raúl Pérez-López¹, José F. Mediato¹, Miguel A. Rodríguez-Pascua¹, Jorge L. Giner-Robles², Adrià Ramos¹, Silvia Martín-Velázquez³, Roberto Martínez-Orío¹, Paula Fernández-Canteli¹

1. IGME – Instituto Geológico y Minero de España – Geological Survey of Spain. C/Ríos Rosas 23, Madrid 28003 – SPAIN. Email: r.perez@igme.es, jf.mediato@igme.es, ma.rodriguez@igme.es, a.ramos@igme.es, ro.martinez@igme.es, paula.canteli@igme.es

2. Departamento de Geología y Geoquímica. Facultad de Ciencias. Universidad Autónoma de Madrid. Campus Cantoblanco, Madrid. SPAIN. Email: jorge.giner@uam.es

3. Universidad Rey Juan Carlos. Email: silvia.martin@urjc.es

Abstract

One of the concerns of underground CO₂ onshore storage is the triggering of Induced Seismicity and fault reactivation by pore pressure increasing. Hence, a comprehensive analysis of the tectonic parameters involved in the storage rock formation is mandatory for safety management operations. Unquestionably, active faults and seal faults depicting the storage bulk are relevant parameters to be considered. However, there is a lack of analysis of the active tectonic strain field affecting these faults during the CO₂ storage monitoring. The advantage of reconstructing the tectonic field is the possibility to determine the strain trajectories and describing the fault patterns affecting the reservoir rock. In this work, we adapt a methodology of systematic geostructural analysis to the underground CO₂ storage, based on the calculation of the strain field and defined by the strain field from kinematics indicators on the fault planes (e_y and e_x for the maximum and minimum horizontal shortening respectively). This methodology is based on statistical analysis of individual strain tensor solutions obtained from fresh outcrops from Triassic to Miocene. Consequently, we have collected 447 fault data in 32 field stations located within a 20 km radius. The understanding of the fault sets role for underground fluid circulation can also be established, helping for further analysis about CO₂ leakage and seepage. We have applied this methodology to Hontomín

32 onshore CO₂ storage facilities (Central Spain). The geology of the area and the number
33 of high-quality outcrops, made this site as a good candidate for studying the strain field
34 from kinematics fault analysis. The results indicate a strike-slip tectonic regime with the
35 maximum horizontal shortening with N160°E and N50°E trend for local regime, which
36 activates NE-SW strike-slip faults. A regional extensional tectonic field was also
37 recognized with N-S trend, which activates N-S extensional faults, and NNE-SSW and
38 NNW-SSE strike-slip faults, measured in the Cretaceous limestone on top of the
39 Hontomín facilities. Monitoring these faults within the reservoir is suggested in addition
40 with the possibility of obtaining focal mechanism solutions for microearthquakes ($M <$
41 3).

42

43 Keywords: onshore CO₂ storage, tectonic field, paleostrain analysis, active fault,
44 Hontomín onshore pilot-plant.

45

46 1. INTRODUCTION

47 Industrial made-man activities generate CO₂ that could change the chemical balance of
48 the atmosphere and their relationship with the geosphere. The Geological Carbon
49 Storage (GSC) appears as a good choice to reduce the CO₂ gas emission to the
50 atmosphere (Christensen, 2004), allowing the industry increasing activity with a low
51 pollution impact. There is a lot of literature about what must have a site to be a potential
52 underground storage suitable to GSC (e.g. Chu, 2009; Orr, 2009; Goldberg et al., 2010
53 among others). The reservoir sealing, the caprock, permeability and porosity, plus
54 injection pressure and volume injected, are the main considerations to choose one
55 geological subsurface formation as the CO₂ host-rock. In this frame, the tectonic active
56 field is considered in two principal ways: (1) to prevent the fault activation and

57 earthquakes triggering, with the consequence of leakage and seepage, and (2) the long-
58 term reservoir behavior, understanding as long-term from centennial to millennial time-
59 span. Therefore, what is the long-term behavior of GSC? What do we need to monitor
60 for a safe GSC management? [Winthaegen et al. \(2005\)](#) suggest three subjects for
61 monitoring: (a) the atmosphere air quality near the injection facilities, due to the CO₂
62 toxicity (values greater than 4%, see [Rice, 2003](#) and [Permentier et al., 2017](#)), (b) the
63 overburden monitoring faults and wells and (c) the sealing of the reservoir. The study of
64 natural analogues for GSC is a good strategy to estimate the long-term behavior of the
65 reservoir, considering parameters as the injected CO₂ pressure and volume, plus the
66 brine mixing with CO₂ ([Pearce, 2006](#)). Hence, the prediction of site performance over
67 long timescales also requires an understanding of CO₂ behavior within the reservoir, the
68 mechanisms of migration out of the reservoir, and the potential impacts of a leak on the
69 near surface environment. The assessments of such risks will rely on a combination of
70 predictive models of CO₂ behavior, including the fluid migration and the long-term
71 CO₂-porewater-mineralogical interactions ([Pearce, 2006](#)). Once again, the tectonic
72 active field interacts directly on this assessment. Moreover, the fault reactivation due to
73 the pore pressure increasing during the injection and storage has also to be considered
74 ([Röhmman et al., 2013](#)). Despite the uplift measure by [Röhmman et al. \(2013\)](#) are
75 submillimeter (c.a. 0.021 mm) at the end of the injection processes, given the ongoing
76 occurrence of microearthquakes, long-term monitoring is required. The geomechanical
77 and geological models predict the reservoir behavior and the caprock sealing properties.
78 The role of the faults inside these models is crucial for the tectonic long-term behavior
79 and the reactivation of faults that could trigger earthquakes.

80 Concerning the Induced Seismicity, [Wilson et al. \(2017\)](#) published the Hi-Quake
81 database, with a classification of all man-made earthquakes according to the literature,

82 in an online repository (<https://inducedearthquakes.org/>, last access on May, 2019). This
83 database includes 834 projects with proved Induced Seismicity, where two different
84 cases with earthquakes as large as M 1.7, detected in swarms about 9,500
85 microearthquakes, are related to GSC operations. Additionally, [Foulger et al. \(2018\)](#)
86 pointed out that GSC can trigger earthquakes with magnitudes lesser than M 2, namely
87 the cases described in their work are as great as M 1.8, with the epicenter location 2 km
88 around the facilities. [McNamara \(2016\)](#) described a comprehensive method and
89 protocol for monitoring GSC reservoir for the assessment and management of Induced
90 Seismicity. The knowledge of active fault patterns and the stress/strain field could help
91 on designing monitoring network and identifying those faults capable of triggering
92 micro-earthquakes ($M < 2$) and/or breaking the sealing for leakage (patterns of open
93 faults for low-permeability CO₂ migration).

94 In this work, we propose that the description, the analysis and establishment of the
95 tectonic strain field have to be mandatory for long-term GSC monitoring and
96 management, implementing the fault behavior in the geomechanical models. This
97 analysis does not increase the cost for long-term monitoring, given that they are low-
98 cost and the results are acquired in a few months. Therefore, we propose a methodology
99 based on the reconstruction of the strain field from the classical studies in geodynamics
100 ([Angelier, 1979 and 1984](#); [Reches, 1983](#); [Reches, 1987](#)). As a novelty, we introduce the
101 strain fields (SF) analysis between 20 away from the subsurface reservoir deep
102 geometry, under the area of influence of induced seismicity for fluid injection. The
103 knowledge of the strain field at local scale allows classifying the type of faulting and
104 their role for leakage processes, whilst the regional scale explores the tectonic active
105 faults that could affect the reservoir. The methodology is rather simple, taking measures
106 of slickensides and striations on fault planes to establish the orientation of the maximum

107 horizontal shortening (e_y), and the minimum horizontal shortening (e_x) for the strain
108 tensor. The principal advantage of the SF analysis is the directly classification of all the
109 faults involved into the geomechanical model and the prediction of the failure
110 parameters. Besides, a Mohr-Coulomb failure analysis was performed to the fault
111 pattern recognized in the Cretaceous outcrop located on top of the pilot plant.

112 The tectonic characterization of the GSC of Hontomín was implemented in the
113 geological model described by [Le Gallo and de Dios \(2018\)](#). Beyond the use of Induced
114 Seismicity and potentially active faults, the scope of this method is to propose an initial
115 analysis to manage underground storage operations. We present how the Structural
116 Analysis of fault/slip data can improve the knowledge of the tectonic large-scale fault
117 network for the potential seismic reactivation during fluid injection and time-depend
118 scale for fluid stays.

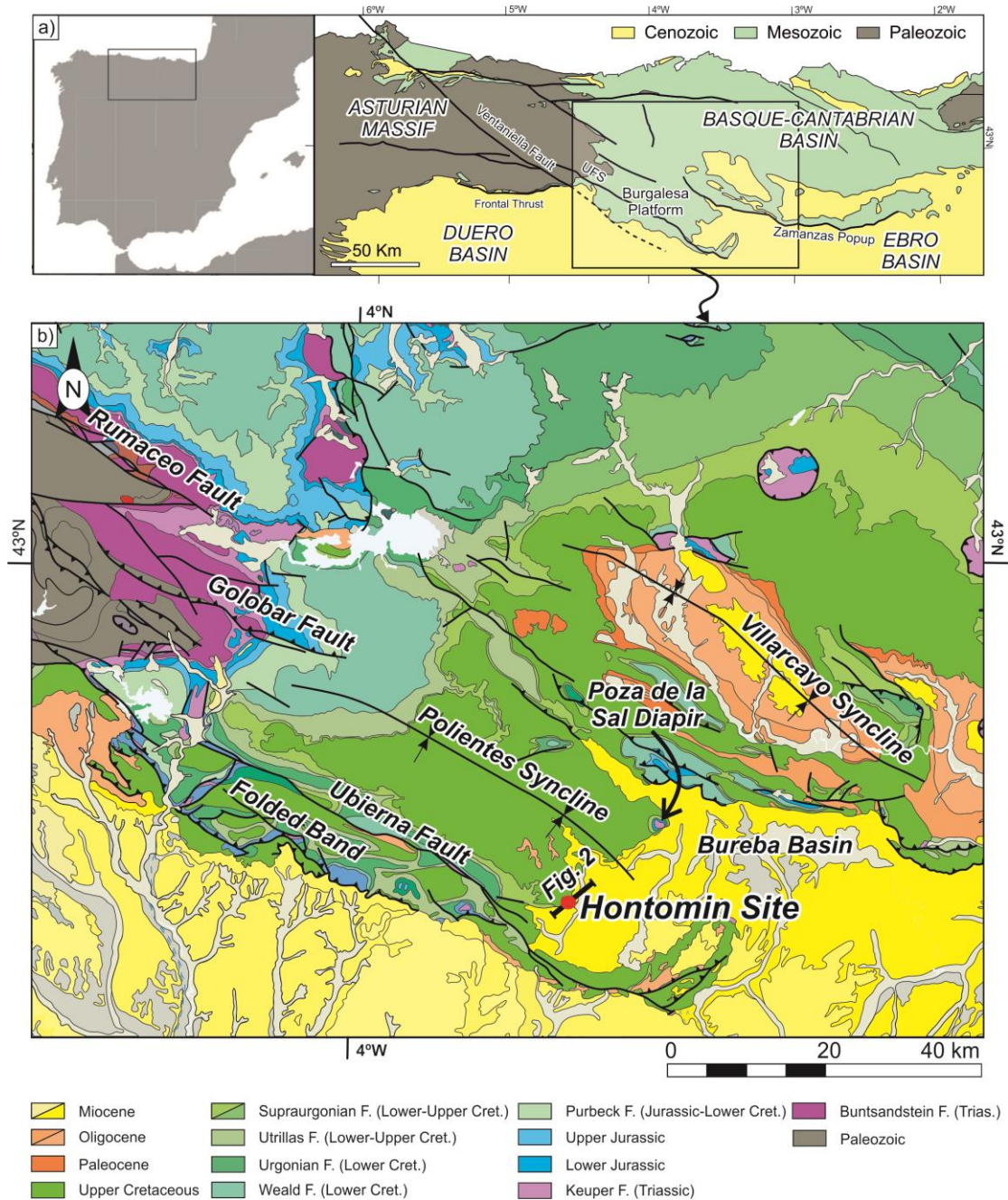
119

120 2. HONTOMÍN ONSHORE STUDY CASE

121 2.1 Geological description of the reservoir

122 The CO₂ storage site of Hontomín is enclosed in the southern section of the Mesozoic
123 Basque–Cantabrian Basin, known as Burgalesa Platform ([Serrano and Martínez del](#)
124 [Olmo, 1990](#); [Tavani, 2012](#)), within the sedimentary Bureba Basin (**Fig. 1**). This
125 geological domain is located in the northern junction of the Cenozoic Duero and Ebro
126 basins, forming an ESE-dipping monocline bounded by the Cantabrian Mountains
127 Thrust to the north, the Ubierna Fault System (UFS) to the south and the Asturian
128 Massif to the west (**Fig. 1**).

129 The Meso-Cenozoic tectonic evolution of the Burgalesa Platform starts with a first rift
130 period during Permian and Triassic times ([Dallmeyer and Martínez-García, 1990](#);
131 [Calvet et al., 2004](#)), followed by a relative tectonic quiescence during Early and Middle



132

133

134

135

136

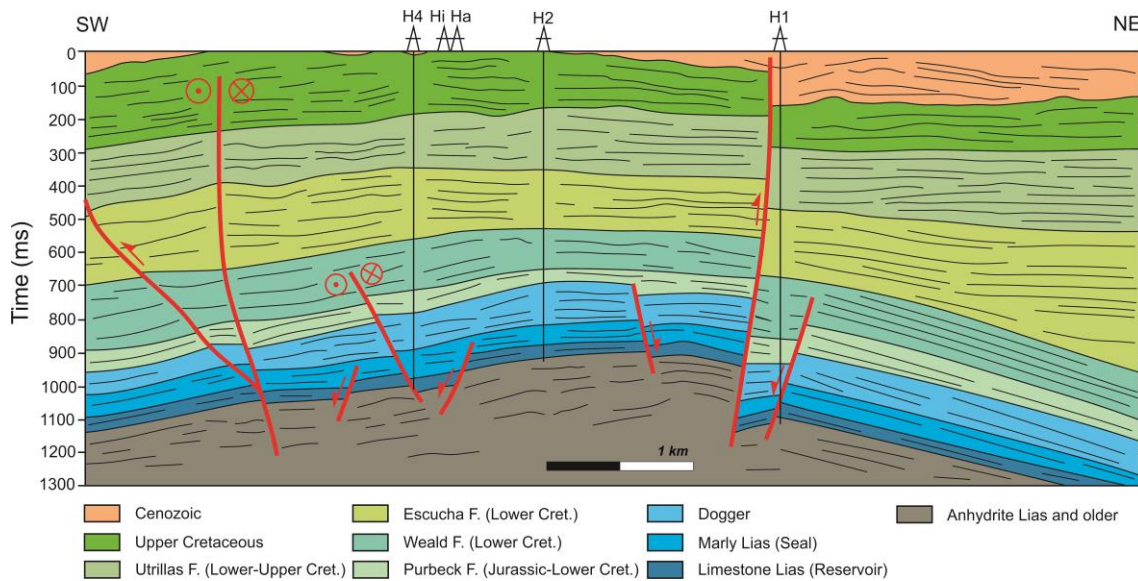
137

138

139

140

Figure 1. a) Location map of the study area in the Iberian Peninsula, along with the geological map of the Asturian and Basque-Cantabrian areas, labelling major units and faults (modified after Quintà and Tavani 2012); b) Geographical location of Hontomín pilot-plant (red dot) within the Basque-Cantabrian Basin. This basin is tectonically controlled by the Ubierna Fault System (UFS; NW-SE oriented) and the parallel Polientes syncline, the Duero and Ebro Tertiary basins and Poza de la Sal evaporitic diapir. Cret: Cretaceous; F: Facies.



141

142

143 **Figure 2.** Interpretation of a 2D seismic reflection profile crossing the oil exploration
 144 wells (H1, H2 and H4), along with the monitoring well (Ha) and injection well (Hi)
 145 through Hontomin Pilot Plant (HPP). Modified from Alcalde et al. (2014). See Figure 1
 146 for location, black line at the red circle.

147

148 Jurassic times (e.g. Aurell et al., 2002). The main rifting phase took place during the
 149 Late Jurassic and Early Cretaceous times, due to the opening of the North Atlantic and
 150 the Bay of Biscay-Pyrenean rift system (García-Mondéjar et al., 1986; Le Pichon and
 151 Sibuet, 1971; Lepvrier and Martínez-García, 1990; García-Mondéjar et al., 1996; Roca
 152 et al., 2011; Tugend et al., 2014). The convergence between Iberia and Eurasia from
 153 Late Cretaceous to Miocene times triggered the inversion of previous Mesozoic
 154 extensional faults and the development of an E-W orogenic belt (Cantabrian domain to
 155 the west and Pyrenean domain to the east) formed along the northern Iberian plate
 156 margin (Muñoz, 1992; Gómez et al., 2002; Vergés et al., 2002).

157 The Hontomín facilities are located within the Basque-Cantabrian Basin (**Fig. 1b**). The
 158 geological reservoir structure is bordered by the UFS to the south and west, by the Poza
 159 de la Sal diapir and the Zamanzas Pop-up structure (Carola, 2014) to the north and by the
 160 Ebro Basin to the east (**Fig. 1**). The structure is defined as a forced fold related dome

161 structure (Tavani et al., 2013; Fig. 2), formed by an extensional fault system with
162 migration of evaporites towards the hanging wall during the Mesozoic (Soto et al.,
163 2011). During the tectonic compressional phase, associated with the Alpine Orogeny
164 affecting the Pyrenees, the right-lateral transpressive inversion of the basement faults
165 was activated, along with the reactivation of transverse extensional faults (Fig. 2;
166 Tavani et al., 2013; Alcalde et al., 2014).

167 The target reservoir and seal formations consist of Lower Jurassic marine carbonates,
168 arranged in an asymmetric dome-like structure (Fig. 2) with an overall extent of 15 km²
169 and located at 1,485 m of depth (Alcalde et al., 2013, 2014; Ogaya et al., 2013). The
170 target CO₂ injection point is a saline aquifer formed by a dolostone unit, known as
171 “Carniolas”, and an oolitic limestone of the Sopeña Formation, both corresponding to
172 Lias in time (Early Jurassic). The estimated porosity of the Carniolas reaches over 12%
173 (Ogaya et al., 2013; Le Gallo and de Dios, 2018) and it is slightly lower at the
174 Carbonate Lias level (8.5% in average). The reservoir levels contain saline water with
175 more than 20 g/l of NaCl and very low oil content. The high porosity of the lower part
176 of the reservoir (i.e., the Carniolas level) is the result of secondary dolomitization and
177 different fracturing events (Alcalde et al., 2014). The minimum thickness of the
178 reservoir units is 100 m. The potential upper seal unit comprises Lias marlstones and
179 black shales from a hemipelagic ramp (Fig. 2); Pliensbachian and Toarcian) of the
180 “Puerto del Pozazal” and Sopeña Formations.

181

182 2.2 Regional tectonic field

183 The tectonic context has been described from two different approaches: (1) the tectonic
184 style of the fractures bordering the Hontomín reservoir (De Vicente et al., 2011; Tavani
185 et al., 2011) and (2) the tectonic regional field described from earthquakes with

186 mechanism solutions and GPS data (Herraiz et al., 2000; Stich et al., 2006; De Vicente
187 et al., 2008).

188 (1) The tectonic style of the Bureba Basin was described by De Vicente et al. (2011),
189 which classified the Basque-Cantabrian Cenozoic Basin (**Fig. 1a**) as transpressional
190 with contractional horsetail splay basin. The NW-SE oriented Ventaniella fault (**Fig.**
191 **1a**), includes the UFS in the southeastward area, being active between the Permian and
192 Triassic period, and strike-slip during the Cenozoic contraction. In this tectonic
193 configuration, the Ubierna Fault acts as a right-lateral strike-slip fault. These authors
194 pointed out the sharp contacts between the thrusts and the strike-slip faults in this basin.
195 Furthermore, Tavani et al. (2011) also described complex Cenozoic tectonic context
196 where right-lateral tectonic style reactivated WNW-ESE trending faults. Both the
197 Ventaniella and the Ubierna faults acted as transpressive structures forming 120 km
198 long and 15 km wide of the UFS, and featured by 0.44 mm/yr of averaged tectonic
199 strike-slip deformation between the Oligocene and the present day. The aforementioned
200 authors described different surface segments of the UFS of right-lateral strike-slip
201 ranging between 12 and 14 km length. The structural data collected by Tavani et al.
202 (2011) pointed out the 60% of data correspond to right lateral strike-slip with WNW-
203 ESE trend, together with conjugate reverse faulting with NE-SW, NW-SE and E-W
204 trend, and left-lateral strike-slip faults N-S oriented. They concluded that this scheme
205 could be related to a transpressional right-lateral tectonic system with a maximum
206 horizontal compression, S_{Hmax} , striking N120°E. Concerning the geological evidence of
207 recent sediments affected by tectonic movements of the UFS, Tavani et al. (2011)
208 suggest Middle Miocene in time for this tectonic activity. However, geomorphic
209 markets (river and valley geomorphology) could indicate tectonic activity at present-
210 times. All of these data correspond to regional or small-scale data collected to explain

211 the Basque-Cantabrian Cenozoic transpressive basin. The advantage of the
212 methodology proposed here to establish the tectonic local regime affecting the reservoir,
213 is the searching for local-scale tectonics (20 km sized), and the estimation of the depth
214 for the non-deformation surface for strata folding in transpressional tectonics (Lisle et
215 al., 2009).

216 (2) Regarding the stress field from earthquake focal mechanism solutions, Herraiz et al.
217 (2000) pointed out the regional trajectories of S_{Hmax} with NNE-SSW trend, and with a
218 NE-SW S_{Hmax} trend from slip-fault inversion data. Stich et al. (2006) obtained the stress
219 field from seismic moment tensor inversion and GPS data. These authors pointed out a
220 NW-SE Africa-Eurasia tectonic convergence at tectonic rate of 5 mm/yr approximately.
221 However, no focal mechanism solutions are found within the Hontomín area (20 km)
222 and only long-range spatial correlation could be made with high uncertainty (in time,
223 space and magnitude). The same lack of information appears in the work of De Vicente
224 et al. (2008), with no focal mechanism solutions in the 50 km surrounding the HPP. In
225 this work, these authors classified the tectonic regime as uniaxial extension to strike-slip
226 with NW-SE S_{Hmax} trend.

227 Regional data about the tectonic field inferred from different works (Herraiz et al.,
228 2000; Stich et al., 2006; De Vicente et al., 2008, 2011; Tavani et al., 2011; Tavani,
229 2012), show differences for the S_{Hmax} . These works explain the tectonic framework for
230 regional scale. Nevertheless, local tectonics could determine the low permeability and
231 the potential induced seismicity within the reservoir. In the next section, we have
232 applied the methodology described at the section 3 of this manuscript, in order to
233 compare the regional results from these works and to establish the tectonic evolution of
234 the Burgalesa Platform.

235

236 2.3 Strategy of the ENOS European Project

237 Hontomín pilot-plant (HPP) for CO₂ onshore storage is the only one in Europe
238 recognized as a key-test-facility, and it is managed and conducted by CIUDEN
239 (*Fundación Ciudad de la Energía*). The HPP is located within the province of Burgos
240 (**Fig. 1b**), in the northern central part of Spain.

241 The methodology proposed in this work and its application for long-term onshore GSC
242 managing in the frame of geological risk, is based on the strain tensor calculation, as
243 part of the objectives proposed in the European project “ENabling Onshore CO₂
244 Storage in Europe” (ENOS). The ENOS project is an initiative of CO₂GeoNet, the
245 European Network of Excellence on the geological storage of CO₂ for supporting
246 onshore storage and fronting the associated troubles as GSC perception, the safe storage
247 operation, potential leaking management and health, and environmental safety ([Gastine
248 et al., 2017](#)). ENOS combines a multidisciplinary European project, which focuses in
249 onshore storage, with the demonstration of best practices through pilot-scale projects in
250 the case of Hontomín facilities. Moreover, this project claims for creating a favorable
251 environment for GSC onshore through public engagement, knowledge sharing, and
252 training ([Gastine et al., 2017](#)). In this context, the work-package WP1 is devoted to
253 “ensuring safe storage operations”.

254

255 3. METHODS AND RATIONALE

256 The lithosphere remains in a permanent state of deformation, related to plate tectonics
257 motion. Strain and stress fields are the consequence of this deformation on the upper
258 lithosphere, arranging different fault patterns that determine sedimentary basins and
259 geological formations. Kinematics of these faults describes the stress/strain fields, for
260 example measuring grooves and slickensides on fault planes (see [Angelier, 1979](#),

261 [Reches, 1983 among others](#)). The relevance of the tectonic field is that stress and strain
262 determine the earthquake occurrence by the fault activity. In this work, we have
263 performed a brittle analysis of the fault kinematics, by measuring slickenfiber on fault
264 planes (dip/ dip direction and rake), in several outcrops in the surroundings of the
265 onshore reservoir. To carry out the methodology proposed in this work, the study area
266 was divided in a circle with four equal areas, and we searched outcrops of fresh rock to
267 perform the fault kinematic analysis. This allows establishing a realistic tectonic very-
268 near field to be considered during the storage seismic monitoring and long-term
269 management. Finally, we have studied the fault plane reactivation by using the Mohr-
270 Coulomb failure criterion (Pan et al., 2016), from the fault pattern obtained in the
271 Cretaceous limestone outcrop located on top of the HPP facilities.

272

273 3.1 *Paleostrain Analysis*

274 We have applied the strain inversion technique to reconstruct the tectonic field
275 (paleostrain evolution), affecting the Hontomín site between the Triassic, Jurassic,
276 Cretaceous and Neogene ages (late Miocene to present times). For a further
277 methodology explanation, see [Etchecopar et al. \(1981\)](#), [Reches \(1983\)](#) and [Angelier](#)
278 [\(1990\)](#). The main assumption for the inversion technique of fault population is the self-
279 similarity to the scale invariance for the stress/strain tensors. This means that we can
280 calculate the whole stress/strain fields by using the slip data on fault planes and for
281 homogeneous tectonic frameworks. The strain tensor is an ellipsoid defined by the
282 orientation of the three principal axes and the shape of the ellipsoid (k). This method
283 assumes that the slip-vectors, obtained from the pitch of the striation on different fault
284 planes, define a common strain tensor or a set in a homogeneous tectonic arrangement.
285 We assume that the strain field is homogeneous in space and time, the number of faults

286 activated is greater than five and the slip vector is parallel to the maximum shear stress
287 (τ).

288 The inversion technique is based on the Bott equations (Bott, 1959). These equations
289 show the relationship between the orientation and the shape of the stress ellipsoid:

290

$$291 \quad \tan(\theta) = [n / (1 * m)] * [m^2 - (1 - n^2) * R'] \quad [\text{eq.1}]$$

$$292 \quad R' = (\sigma_z - \sigma_x) / (\sigma_y - \sigma_x) \quad [\text{eq.2}]$$

293

294 Where l, m and n are the direction cosines of the normal to the fault plane, θ is the pitch
295 of the striation and R' is the shape of the stress ellipsoid obtained in an orthonormal
296 coordinate system, x, y, z. In this system, σ_y is the maximum horizontal stress, σ_x is the
297 minimum horizontal stress axis and σ_z is the vertical stress axis.

298

299 *3.2 The Right-Dihedral Model for Paleostrain Analysis*

300 The Right-Dihedral (RD) is a semi-quantitative method based on the overlapping of
301 compressional and extensional zones by using a stereographic plot. The final plot is an
302 interferogram figure, which usually defines the strain-regime. This method is strongly
303 robust for conjugate fault sets and with different dip values for a same tensor. The RD
304 was originally defined by Pegoraro (1972) and Angelier and Mechler (1977), as a
305 geometric method, adjusting the measured fault-slip data (slickensides) in agreement
306 with theoretical models for extension and compressive fault-slip. Therefore, we can
307 constraint the regions of maximum compression and extension related to the strain
308 regime.

309

310 *3.3 The Slip Model for the Paleostrain Analysis*

311 The Slip Model (SM) is based on the Navier-Coulomb fracturing criteria (Reches,
312 1983), taking the Anderson model solution for this study (Anderson, 1951; Simpson,
313 1997). The Anderson model represents the geometry of the fault plane as monoclinic,
314 relating the quantitative parameters of the shape parameter (K') with the internal
315 frictional angle for rock mechanics (ϕ) (De Vicente 1988; Capote et al., 1991).
316 Moreover, this model is valid for neofomed faults, and some considerations have to be
317 accounted for previous faults and weakness planes present in the rock. These
318 considerations are related to the dip of normal and compressional faults, such as for
319 compressional faulting dip values lower than 45° , reactivated as extensional faults. This
320 model shows the relationships between the K' , ϕ and the direction cosines for the
321 striation on the fault plane (De Vicente, 1988; Capote et al., 1991):

322

$$323 \quad K' = e_y / e_z \quad [eq.3]$$

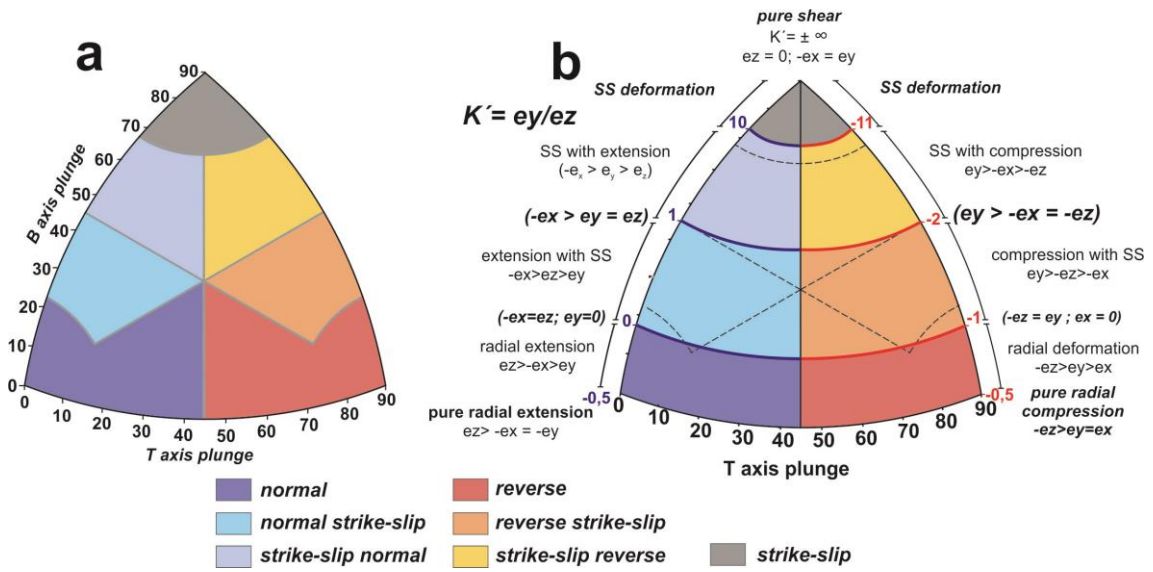
324

325 Where e_z is the vertical strain axis, e_y is the maximum horizontal shortening and e_x is
326 the minimum horizontal shortening. This model assumes that there is no change of
327 volume during the deformation and $e_y = e_x + e_z$.

328 For isotropic solids, principal strain axes coincide with the principal stress axes. This
329 means that in this work, the orientation of the principal stress axis, S_{Hmax} is parallel to
330 the orientation of the principal strain axes, e_y , and hence, the minimum stress axis, S_{hmin} ,
331 is parallel to the minimum strain axis, e_x . This assumption allows us to estimate the
332 stress trajectories (S_{Hmax} and S_{hmin}) from the e_y SM results.

333 Resolving the equations of Anderson for different values (Anderson, 1951), we can
334 classify the tectonic regime that activates one fault from the measurement of the fault
335 dip, sense of dip (0° - 360°) and pitch of the slickenside, assuming that one of the

336 principal axes (e_x , e_y or e_z) is vertical (Angelier, 1984). We can classify the tectonic
 337 regime and represent the strain tensor by using the e_y and e_x orientation.



338 **Figure 3.** a) Kaverina original diagram to represent the tectonic regime from an
 339 earthquake focal mechanism population (see Kaverina et al., 1996 and Álvarez-Gómez,
 340 2014). b) K' -strain diagram used in this work. Dotted lines represent the original
 341 Kaverina limits. Colored zones represent the type of fault. The tectonic regime is also
 342 indicated by the relationship between the strain axes and the colored legend. SS Strike
 343 slip. The B axis is the orthogonal to the P and T axes.
 344
 345

346 3.4 The K' strain diagram

347 Another analysis can be achieved by using the K' -strain diagram developed by Kaverina
 348 et al. (1996) and codified in python-code by Álvarez-Gómez (2014). These authors have
 349 developed a triangular representation based on the fault-slip, where tectonic patterns can
 350 be discriminated between strike-slip and dip-slip types. This diagram is divided in 7
 351 different zones according to the type of fault: (1) pure normal, (2) pure reverse and (3)
 352 pure strike-slip; combined with the possibility of oblique faults: (4) reverse strike-slip
 353 and (5) strike-slip with reverse component; and lateral faults: (6) normal strike-slip and
 354 (7) strike-slip faults with normal component (Fig. 3). Strike-slip faults are defined by
 355 small values for pitch ($p < 25^\circ$), and dips close to vertical planes ($\beta > 75^\circ$). High pitch

356 values ($p > 60^\circ$) are related to normal or/reverse fault-slip vectors. Extensional faults
357 show e_y in vertical whereas compressional faults show e_y in horizontal plane.

358 This method was originally performed for earthquake focal mechanism solutions by
359 using the focal parameters, the nodal planes (dip and strike) and rake (Kaverina et al.,
360 1996). The triangular graph is based on the equal-area representation of the T, N or B
361 and P axes in spherical coordinates (T tensile, N or B neutral and P pressure axes), and
362 the orthogonal regression between earthquake magnitudes M_s and m_b for the Harvard
363 earthquake CMT global catalogue in 1996. [Álvarez-Gómez \(2014\)](#) presented a code
364 python-based for computing the Kaverina diagrams, and we have modified the input
365 parameters by including the K' intervals for the strain field from the SM. The
366 relationship between the original diagram of Kaverina (**Fig. 3a**) and the K' -dip diagram
367 (**Fig. 3b**) that we have used in this work is shown in the figure 3. The advantage of this
368 diagram is the fast assignation of the type of fault and the tectonic regime that determine
369 this fault pattern, and the strain axes relationship.

370 Table 1 summarizes the different tectonic regimes of the figure 3b showing the
371 relationship with the strain main axes e_y , e_x and e_z . This diagram exhibits a great
372 advantage to classify the type of fault according to the strain tensor. Therefore, we can
373 assume the type of fault from the fault orientation affecting geological deposits for each
374 strain tensor obtained.

375

376 *3.5 The Circular-Quadrant-Search (CQS) strategy for the paleostain analysis*

377 In this work, we propose a low-cost strategy based on a well-known methodology for
378 determining the stress/strain tensor affecting a GSC reservoir, which will allow the
379 long-term monitoring of the geological and seismic behavior (**Fig. 4**). The objective is
380 to obtain enough structural data and spatially homogeneous of faults (**Figs. 4, 5**) for
381 reconstructing the stress/strain tensor. The key-point is the determination of the

382 orientation of the e_y , e_x and K' to plot in a map and therefore, to establish the tectonic
 383 regime. We have chosen quadrants of the circles with the aim to obtain a high-quality
 384 spatial distribution of point for the interpretation of the local and very near strain field.
 385 Hence, data are homogeneously distributed, instead of being only concentrated in one
 386 quadrant of the circle.

K'	T -axis	strain axis rel.	fault type	tectonic field
< -0.5	0°	$e_z > -e_x = -e_y$	normal	pure radial extension
$-0.5 < K' < 0$	$0^\circ-45^\circ$	$e_z > -e_x > -e_y$	normal	radial extension
$K' = 0$	$0^\circ-45^\circ$	$e_z = -e_x; e_y = 0$	normal	plain strain
$0 < K' < 1$	$0^\circ-45^\circ$	$-e_x > e_z > e_y$	normal with SS	extension with shear
$k=1$	$0^\circ-45^\circ$	$-e_x > e_y = e_z$	normal with SS	extension with shear
$1 < K' < 10$	$0^\circ-45^\circ$	$-e_x > e_y > e_z$	strike-slip with N	shear with extensional
$10 < K' < \infty$	$0^\circ-45^\circ$	-----	strike-slip	shear deformation
$K' = \infty$	45°	$e_z = 0; -e_x = e_y$	strike-slip	pure shear deformation
$\infty < K' < -11$	$45^\circ-90^\circ$	-----	strike-slip	shear deformation
$-11 < K' < -2$	$45^\circ-90^\circ$	$e_y > -e_x > -e_z$	strike-slip with R	shear with compression
$K' = -2$	$45^\circ-90^\circ$	$e_y > -e_x = -e_z$	reverse with SS	compression with shear
$-2 < K' < -1$	$45^\circ-90^\circ$	$e_y > -e_x > -e_z$	reverse with SS	compression with shear
$K' = -1$	$45^\circ-90^\circ$	$-e_z = e_y; e_x = 0$	reverse	plain strain
$-1 < K' < -0.5$	$45^\circ-90^\circ$	$-e_z > e_y > e_x$	reverse	radial compression
$K' = -0.5$	$45^\circ-90^\circ$	$-e_z > e_y = e_x$	reverse	pure radial compression

SS = strike-slip
 N = normal
 R = reverse
 e_x = value of the minimum horizontal shortening
 e_y = value of the maximum horizontal shortening
 e_z = value of the vertical axis

387

388 **Table 1.** Different tectonic regimes, K' values, dip values and fault type for the
 389 Kaverina modified diagram used in this work. According to the strain axes relationship,
 390 faults can be classified and the tectonic regime can be established.

391

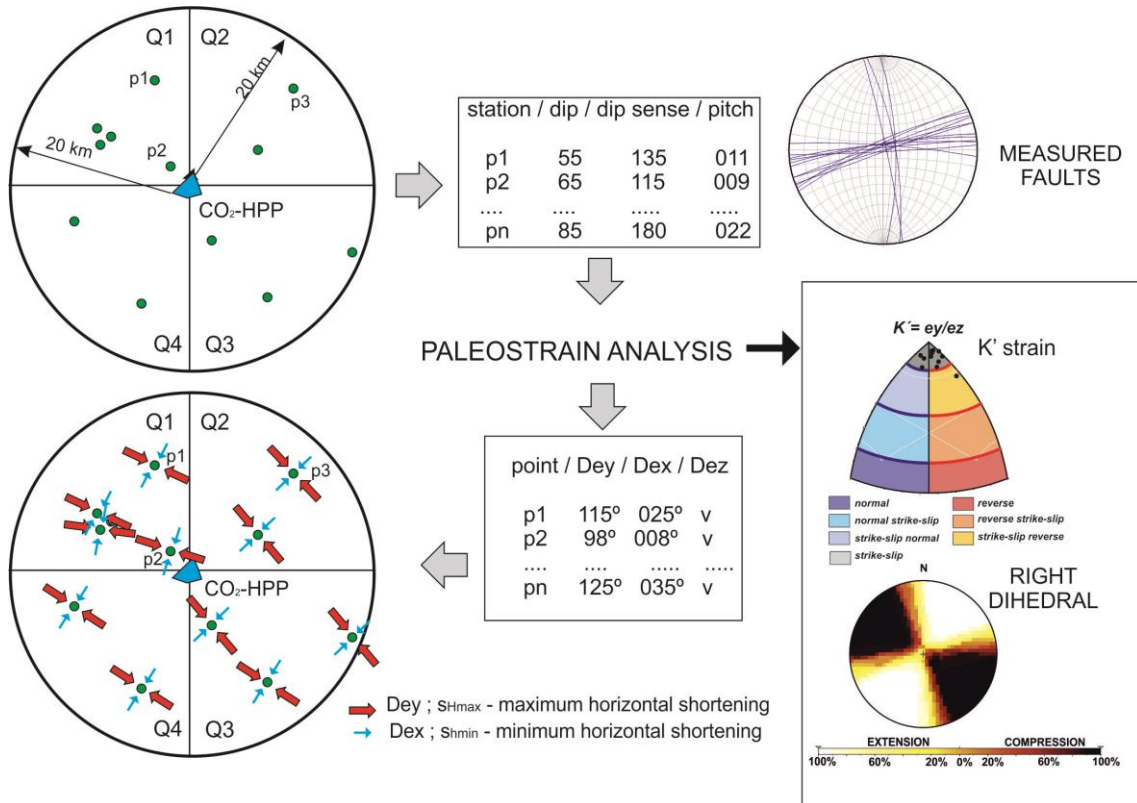
392 Pérez-López et al. (2018) carried out a first approach to the application of this
 393 methodology at Hontomín, under the objective of the ENOS project (see next section
 394 for further details). We propose a circular searching of structural field stations (Figs. 4,
 395 5), located within a 20 km radius. This circle was taken, given that active faults with the
 396 capacity of triggering earthquakes of magnitudes close to M 6, exhibits a surface rupture
 397 of tens of kilometers, according to the empirical models (Wells and Coppersmith,
 398 1994). Moreover, Verdon et al. (2015) pointed out that the maximum distance of
 399 induced earthquakes for fluid injection is 20 km. Larger distances could not be related
 400 to the stress/strain regime within the reservoir, except for the case of large geological

401 structures (folds, master faults, etc.). Microseismicity in GSC reservoir is mainly related
402 to the operations during the injection/depletion stages and long-term storage (Verdon
403 2014; Verdon et al., 2015; McNamara, 2016).

404 The presence of master faults (capable to trigger earthquakes of magnitude = or > than 6
405 and 5 km long segment) inside the 20 km radius circle, implicates that the regional
406 tectonic field determines the strain accumulation in kilometric fault-sized. Furthermore,
407 the presence of master faults could increase the occurrence of micro-earthquakes, due to
408 the presence of secondary faults prone to trigger earthquakes by their normal seismic
409 cycle (Scholz, 2018). Bearing in mind that GSC onshore reservoirs use to be deep saline
410 aquifers (e.g. Bentham and Kirby, 2005) as the Hontomín case (Gastine et al., 2017, Le
411 Gallo and de Dios, 2018), which is confined in folded and fractured deep geological
412 structures, in which local tectonics plays a key role in micro-seismicity and the
413 possibility of CO₂ leakage.

414 The constraints of this strategy are related to the absence of kinematics indicators on
415 fault planes. It could occur due to later overlapping geological processes as neoformed
416 mineralization. Also, a low rigidity eludes the slicken fiber formation, and no
417 kinematic data will be marked on the fault plane.. A poor spatial distribution of the
418 outcrops was also taken into account for constraining the strategy. The age of sediments
419 does not represent the age of the active deformations and hence, the active deformation
420 has to be analyzed by performing alternative methods (i.e. paleoseismology,
421 archaeoseismology).

422



423

424

425 **Figure 4.** Methodology proposed to obtain the strain field affecting the GSC reservoir.
 426 The distances for outcrops and quadrants proposed is 20 km. The technique of Right
 427 Dihedral and the K' strain diagram is described in the main text. The ey and ex
 428 represented are a model for explaining the methodology. Dey and Dex are the direction
 429 of the maximum and minimum strain, respectively. Blue box at the center is the CO₂
 430 storage geological underground formation.

431

432 4. RESULTS

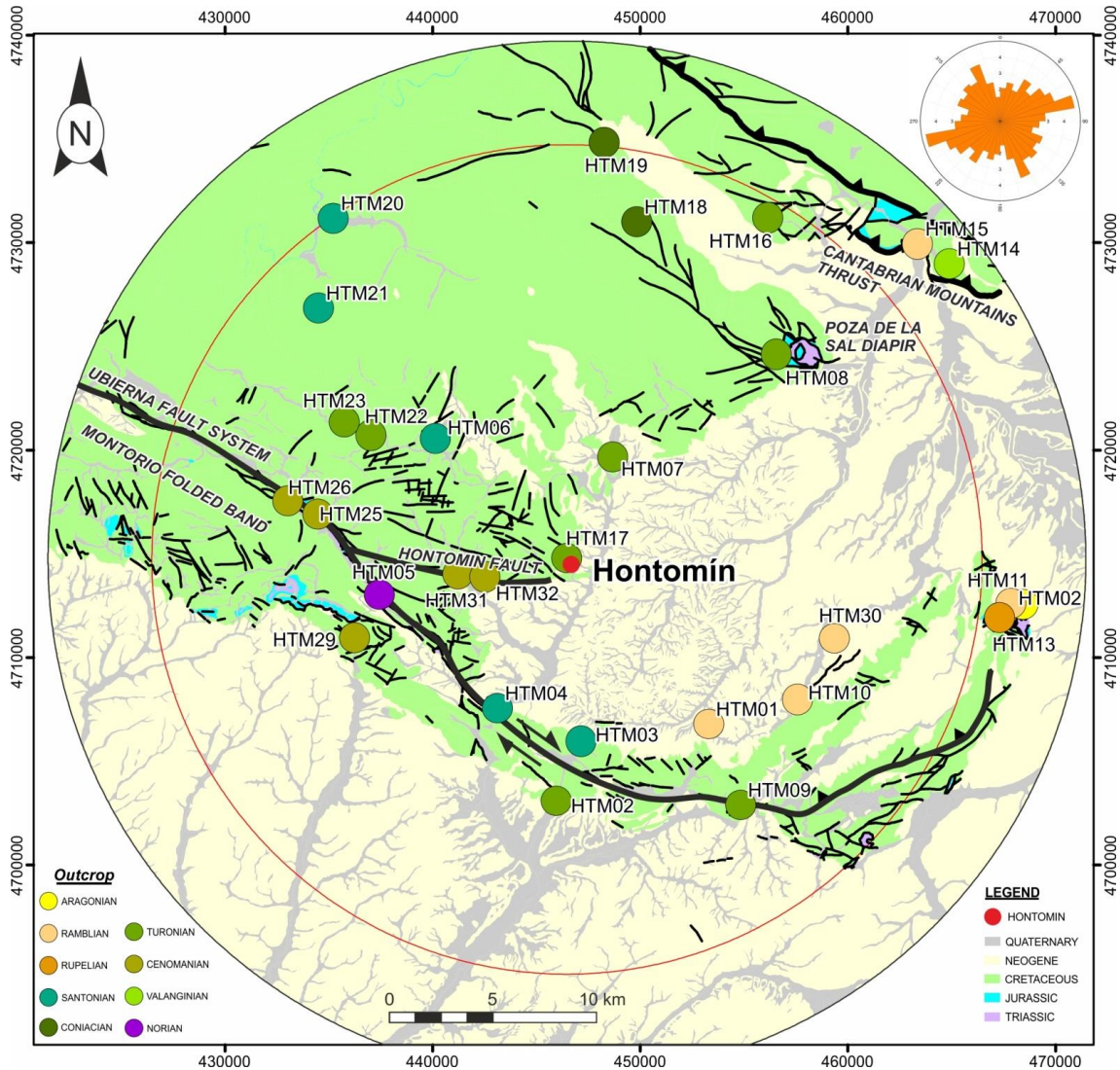
433 4.1 Strain Field Analysis

434 We have collected 447 fault-slip data on fault planes in 32 outcrops, located within a 20
 435 km radius circle centered at the HPP (**Fig. 5**). The age of the outcrops ranges between
 436 Early Triassic to post-Miocene and are mainly located in Cretaceous limestone and
 437 dolostone (**Fig. 5, Table 2**). However, no Jurassic outcrops were located, and only
 438 seven stations are located on Neogene sediments, ranging between Early Oligocene to
 439 Middle-Late Miocene. The small number of Neogene stations is due to the mechanical

440 properties of the affected sediments, mainly poor-lithified marls and soft-detrital fluvial
441 deposits. Despite that, all the Neogene stations exhibit high-quality data with a number
442 of fault-slip data ranging between 7 and 8, enough for a minimum quality analysis.

443 We have labeled the outcrops with the acronym HTM followed by a number (see **figure**
444 **5** for the geographical location and **Table 2** and **figure 6** for the fault data). The station
445 with the highest number of faults measured is HTM17 with 105 faults on Cretaceous
446 limestone. Conjugate fault systems can be recognized in most of the stations (HTM1, 3,
447 5, 7, 10, 14, 16, 21, 23, 24, 25, 29, 30 and 32, **Fig. 6**), although there are a few stations
448 with only one well defined fault set (6, 22, 32). We have to bear in mind that the
449 recording of conjugate fault systems is more robust for the brittle analysis than
450 recording isolated fault sets, better constraining the solution ([Žaholar and Vrabc, 2008](#)).
451 In total, 29 of 32 stations were used (HTM24, 27, 28 with no quality data), and
452 from these 29 stations, 21 were analyzed with the paleostrain technique. Solutions
453 obtained here are robust to establish the paleostrain field in each outcrop as the
454 orientation of the e_y , S_{Hmax} (**Fig. 7**).

455 The results obtained from the application of the paleostrain method have been expressed
456 in stereogram, right dihedral (RD), slip method (SM) and K' - diagram (**Fig. 7**). The K' -
457 diagram shows the fault classification as normal faults, normal with strike-slip
458 component, pure strike-slip, strike-slip with reverse component and reverse faults (see
459 **Fig. 3**). Main faults are lateral strike-slips and normal faults, followed by reverse faults,
460 strike-slips and oblique strike-slips faults. The results of the strain regime are as
461 follows: 1) 43% of extensional with shear component; 2) 22% of shear; 3) 13% of
462 compressive strain (lower Cretaceous and early-middle Miocene, **Table 2**); 4) 13% of
463 pure shear and 5) 9% of shear with compression strain field, although with the presence
464 of five reverse faults.



465
 466 **Figure 5.** Geographical location of field outcrops in the eastern part of the Burgalesa
 467 Platform domain. Black lines: observed faults; red circle: 20km radius study zone. Rosd
 468 diagram are the fault orientations from the map. A total of 447 fault data were collected
 469 in 32 outcrops. Data were measured by a tectonic compass on fault planes at outcrops.
 470 The spatial distribution of the field stations is constrained by the lithology. Coordinates
 471 are in meters, UTM H30.

472
 473 In contrast, we can observe that there are solutions with a double value for the e_y , S_{Hmax}
 474 orientation: HTM1, 2, 10, 11, 13, 15, 19, 26, and 30. The stations HTM3 and 23 (upper
 475 Cretaceous), show the best solution for strike-slip strain field as a pure strike-slip
 476 regime and e_y with N25°E and N99°E trend, respectively (**Fig. 7**).

477 It is easy to observe the agreement between the e_y results from the SM and the K' - strain
 478 diagram, for instance, in the HTM2 the K' -diagram indicates strike-slip faults with
 479 reverse component for low dips ($0^\circ < \beta < 40^\circ$), but also indicates strike-slip faults with
 480 normal component for larger dips ($40^\circ < \beta < 90^\circ$). However, both results are in
 481 agreement with a strain field defined by the orientation for e_y , S_{Hmax} with $N150^\circ \pm 18^\circ$
 482 trend. This tectonic field affects Cretaceous carbonates and coincides with the regional
 483 tectonic field proposed by Herraiz et al. (2000), Tavani et al. (2011) and Alcalde et al.
 484 (2014).

STATION	nº faults	series/epoch	Dey (°)	dispersion	strain tensor
HTM5	18	UPPER TRIASSIC	140	8	NORMAL STRIKE-SLIP
HTM14	8	LOWER CRETACEOUS	34	21	COMPRESSION
HTM2	34	UPPER CRETACEOUS	150	18	STRIKE-SLIP (N-C)
HTM3	8	UPPER CRETACEOUS	25	6	STRIKE-SLIP (N-C)
HTM08	10	UPPER CRETACEOUS	45	11	STRIKE-SLIP
HTM17	105	UPPER CRETACEOUS	107	24	NORMAL
HTM19	20	UPPER CRETACEOUS	61	30	NORMAL STRIKE-SLIP
HTM20	11	UPPER CRETACEOUS	75	5	STRIKE-SLIP
HTM21	14	UPPER CRETACEOUS	138	22	STRIKE-SLIP NORMAL
HTM22	5	UPPER CRETACEOUS	175	8	NORMAL STRIKE-SLIP
HTM23	14	UPPER CRETACEOUS	99	15	STRIKE-SLIP
HTM25	11	UPPER CRETACEOUS	141	26	STRIKE-SLIP COMPRESSION
HTM26	10	UPPER CRETACEOUS	0	23	STRIKE-SLIP
HTM29	8	UPPER CRETACEOUS	179	24	STRIKE-SLIP NORMAL
HTM31	11	UPPER CRETACEOUS	108	16	STRIKE-SLIP NORMAL
HTM32	6	UPPER CRETACEOUS	90	7	NORMAL
HTM13	24	EARLY OLIGOCENE	25-160	23	NORMAL STRIKE-SLIP
HTM01	7	EARLY-MIDDLE MIOCENE	70	22	NORMAL STRIKE-SLIP
HTM10	8	EARLY-MIDDLE MIOCENE	69	13	NORMAL STRIKE-SLIP
HTM15	13	EARLY-MIDDLE MIOCENE	33	25	COMPRESSION
HTM30	6	EARLY-MIDDLE MIOCENE	145	21	COMPRESSION
HTM11	8	MIDDLE MIOCENE	50	4	NORMAL STRIKE-SLIP

485
 486 **Table 2.** Summary of the outcrops showing the number of faults, the type of the strain
 487 tensor obtained, the Dey, S_{Hmax} striking and the age of the affected geological materials.
 488 N-C is normal component for strike-slip movement.

490 4.2 Late Triassic Outcrop Paleostrain

491 Strain analysis from HTM5 fault set shows e_y with NW-SE trending and shear regime
 492 with extension defined by strike-slip faults (Figs. 7a). This is in agreement with the

493 uniaxial extension described in [Tavani \(2012\)](#), constraining this regime with S_{hmin} with
494 NE-SW trending.

495

496 *4.3 Cretaceous Outcrops Paleostrain*

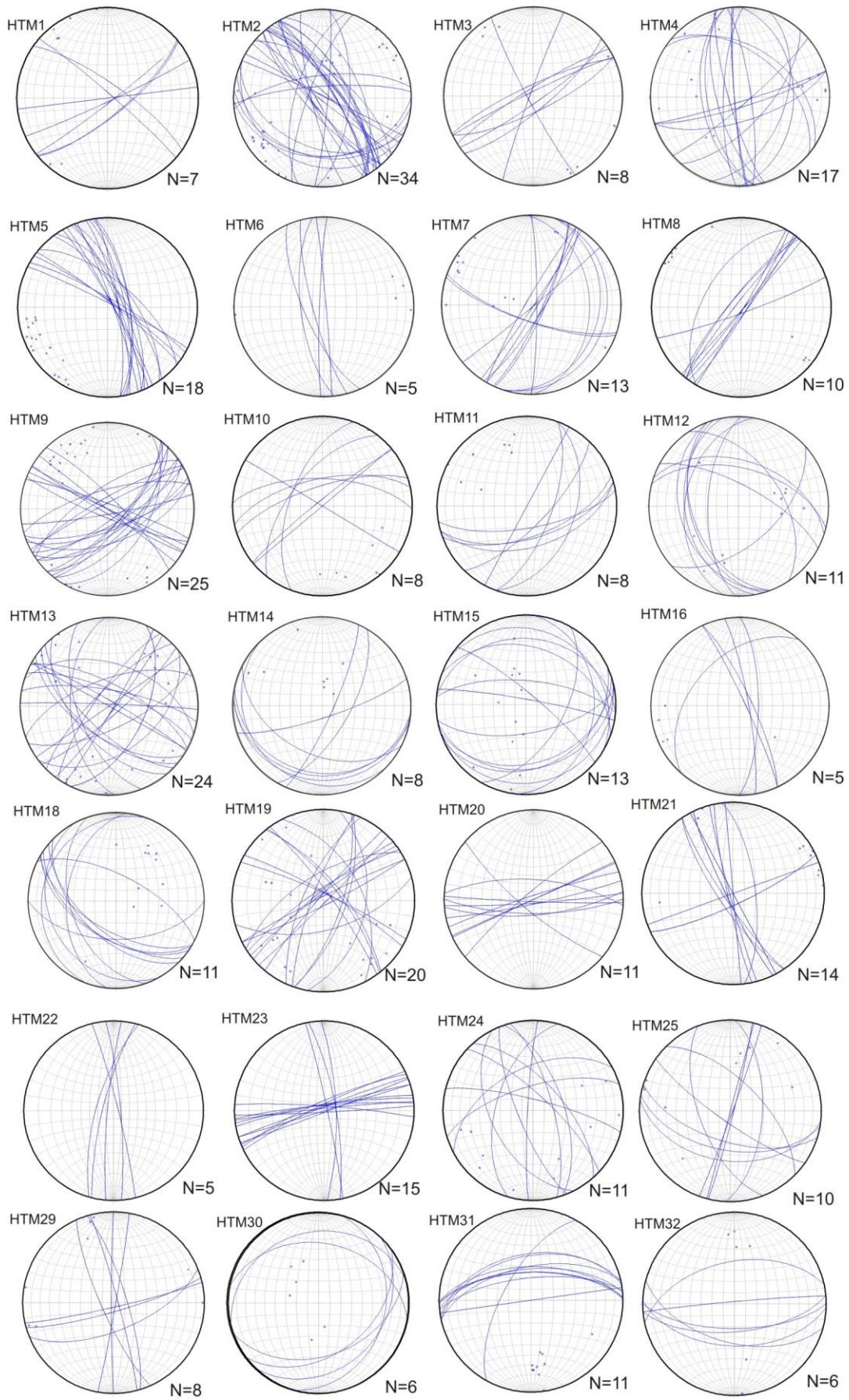
497 We have divided this result in two groups, (a) outcrops within the 20km circle from
498 HPP and (b) the outcrop the HTM17 (**Fig. 5**), which is located in the HPP facilities and
499 described in the next section. HTM14 is the only outcrop from Early Cretaceous age,
500 showing a compressive tectonic stage with reverse fault solutions, defined by e_y with
501 NE-SW trend (**Fig. 7b and 7c**). Taking into account the extensional stage related to the
502 Main Rifting Stage that took place in Early Cretaceous times (i.e. [Carola, 2004](#); [Tavani,](#)
503 [2012](#); [Tugend et al., 2014](#)), we interpreted these results as a modern strain field,
504 probably related to the Cenozoic Inversion stage.

505 Outcrops HTM 2, 3, 8, 17, 19, 20, 21, 22, 23, 25, 26, 29, 31 and 32 are from the upper
506 Cretaceous carbonates (**Fig. 7**). Results are: (1) a compressive strain stage featured by e_y
507 with NW-SE trend, similar to the stage described in [Tavani \(2012\)](#), and (2) a normal
508 strain stage with e_y striking both E-W and NE-SW (**Fig. 7**, HTM 20, 21, 31 and 32).
509 Finally, a (3) shear stage (activated strike-slip faults) and (4) a shear with extension
510 (strike-slip with normal component) were described as well. These two late stages are
511 featured by e_y with NE-SW and NW-SE trends. The existence of four different strain
512 fields is determined by different ages during the Cretaceous and different spatial
513 locations in relation to the main structures, the Ubierna Fault System, Hontomín Fault,
514 Cantabrian Thrust, Montorio folded band and the Polientes syncline (**Fig. 1**).

515

516

517



519 **Figure 6.** Stereographic representation (cyclographic plot in Schmidt net, lower
520 hemisphere) of the fault planes measured in the field stations. “n” is the number of
521 available data for each geostructural station. HTM24, 27, 28 are not included due to
522 lack of data, and HTM17 due to the high number of faults.

523

524 *4.4 Cretaceous Outcrop HTM17 on the Hontomín Pilot Plant*

525 This outcrop is located on top of the geological reservoir, in a quarry of Upper
526 Cretaceous limestones. The main advantage of this outcrop is the well-development of
527 striation and carbonate microfibers which yields high-quality data. 105 fault-slip data
528 were measured, with the main orientation striking N75°E; N-50°E; and a conjugate set
529 with N130°E ($\pm 10^\circ$) trend (**Fig. 8**). The result of the strain inversion technique shows an
530 extensional field featured by an ey trajectory striking N107°E ($\pm 24^\circ$) related to an
531 extensional strain field (see the K' diagram in **figure 8**). Most of the faults are
532 extensional faults NE-SW and NW-SE oriented (**Fig. 9**), in agreement with the
533 extensional RD solution. Reverse faults are oriented NNE-SSW, E-W and WNW-ESE.
534 The advantage of this outcrop is the geographical and stratigraphic position. It is located
535 on top of the HPP facilities in younger sediments than the reservoir rocks. Furthermore,
536 given that the Jurassic reservoir rock and the Cretaceous upper unit are both composed
537 by carbonates, the fault pattern measured here could be a reflex of the fracture network
538 affecting the Jurassic storage rocks in depth (see **Figs. 2, 9**).

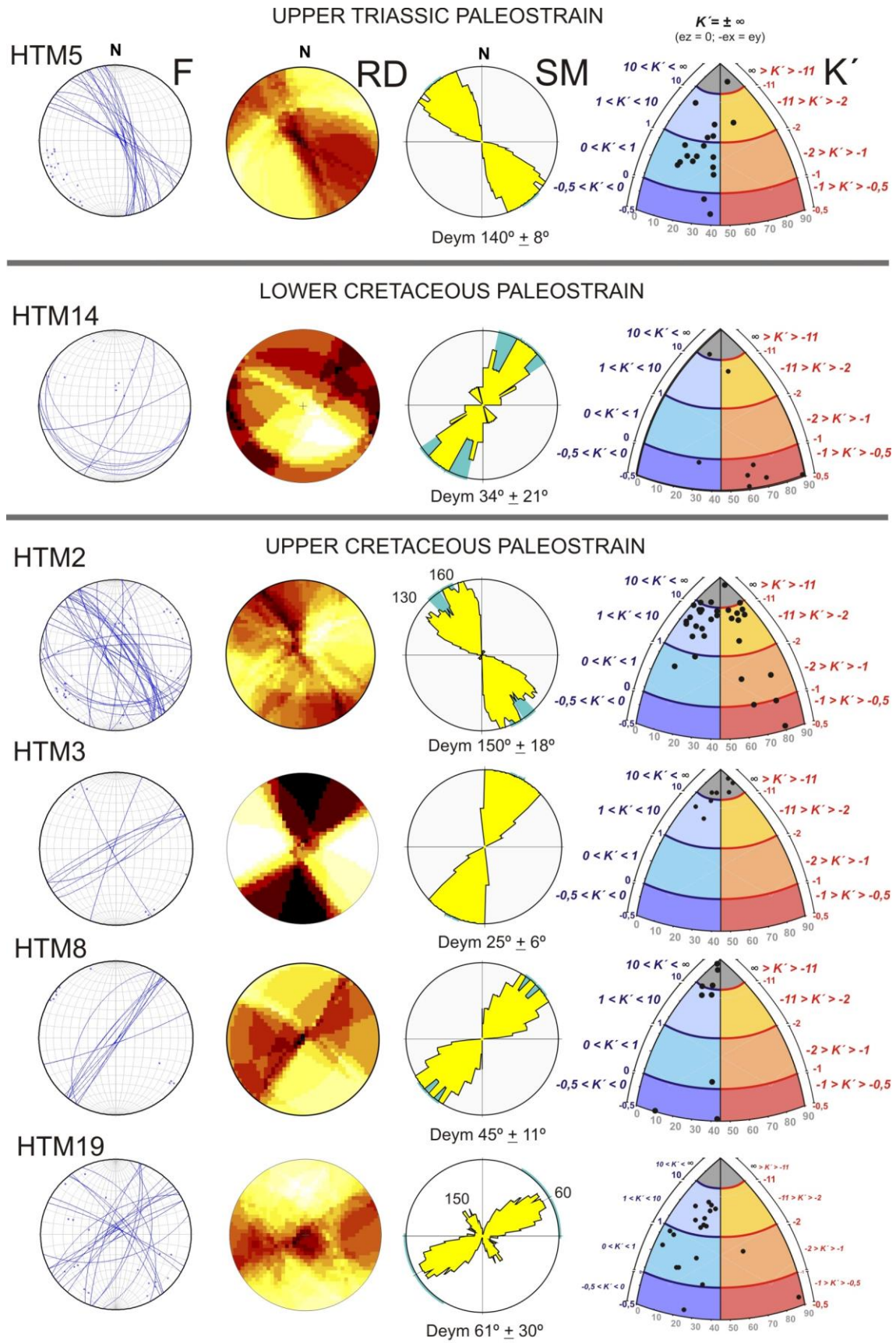


FIGURE 7a

539

540

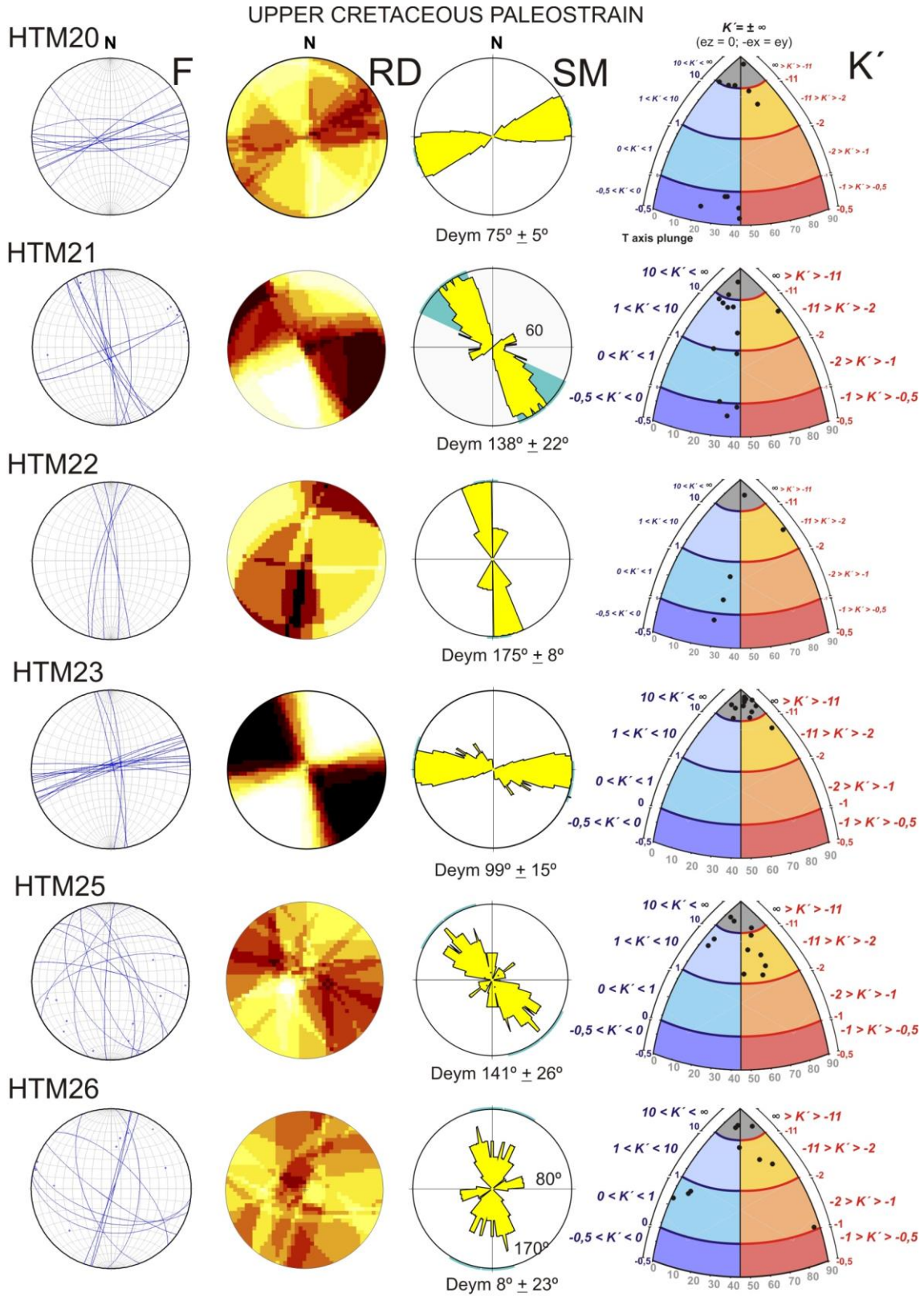
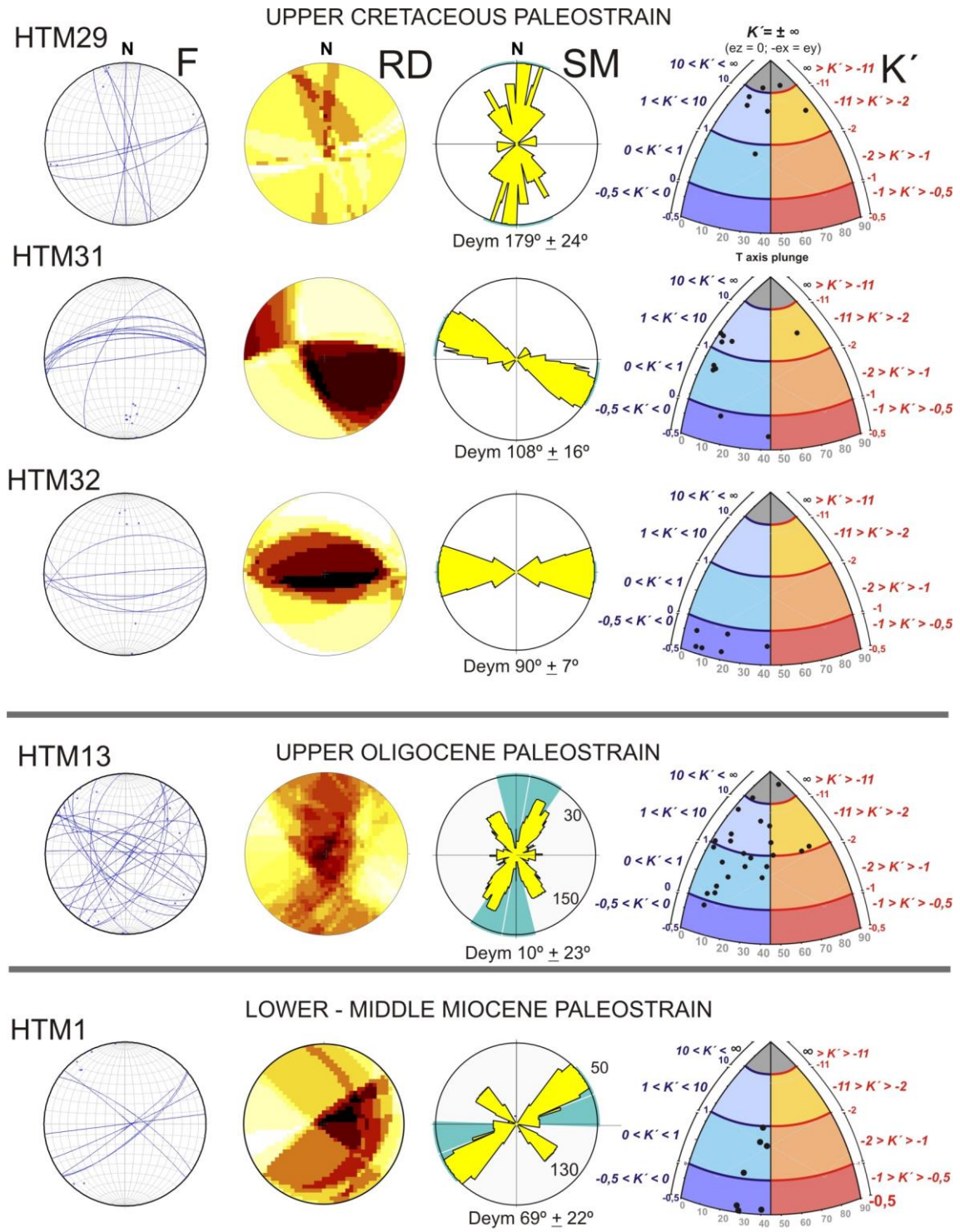


FIGURE 7b

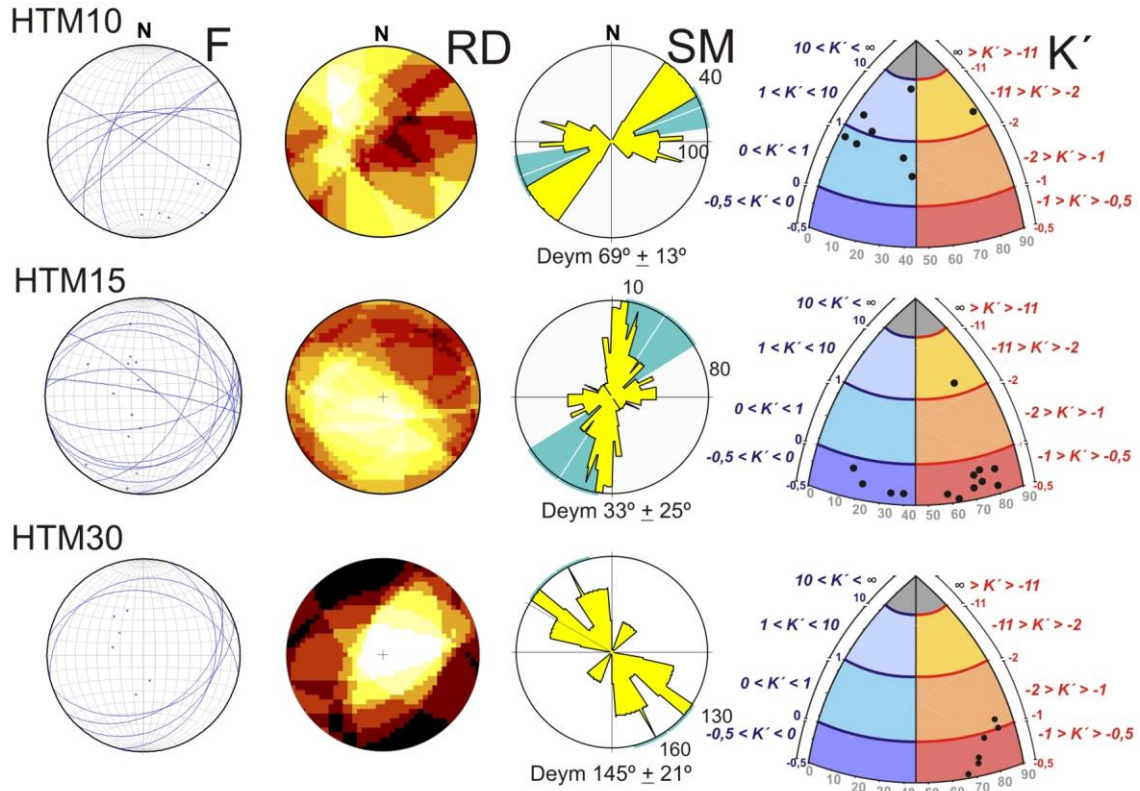
541

542

543



LOWER - MIDDLE MIOCENE PALEOSTRAIN



MIDDLE MIOCENE PALEOSTRAIN

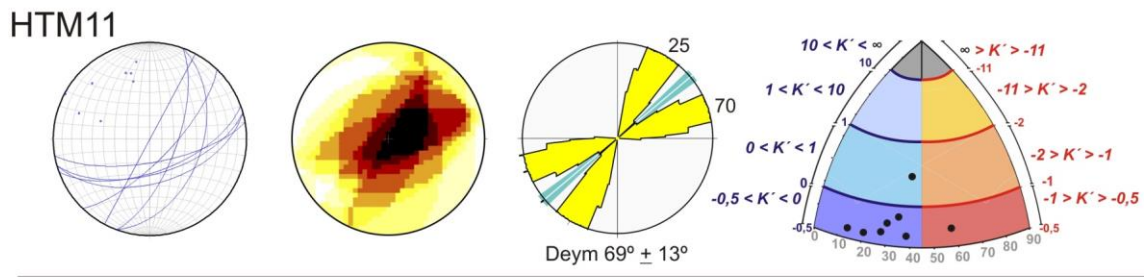


FIGURE 7d

549

550

551 **Figure 7.** Results of the paleostrain analysis obtained and classified by age. Deym:
 552 striking of the averaged of the Dey value; F: fault stereographic representation; K':
 553 diagram with dots for each fault slip solution; RD: Right Dihedral method; SM: Slip
 554 Method, K'. See Methods for further explanation.

555

556

557 *4.5 Cenozoic outcrops strain field*

558 The Cenozoic tectonic inversion was widely described in the area by different authors
559 (e.g. Carola, 2004; Tavani, 2012; Tungend et al., 2014). This tectonic inversion is
560 related to compressive structures, activating NW-SE and NE-SW thrusts with NW-SE
561 and NNE-SSW e_y trends, respectively. The Ubierna Fault has been inverted with a
562 right-lateral transpressive kinematics during the Cenozoic (Tavani et al., 2011). Early
563 Oligocene outcrop (HTM13, **Figs. 7c**) shows a local extensional field with e_y with
564 NNE-SSW and N150°E trend. During the Lower-Middle Miocene, HTM15 and HTM30
565 outcrops exhibit the same e_y trend, but for a compressive tectonic regime (**Figs. 7d**).
566 HTM1 shows extensional tectonics with e_y oriented N50°E and N130°E. Summarizing,
567 the Cenozoic inversion and tectonic compression are detected during the Early to
568 Middle Miocene and the Oligocene. However, during the middle Miocene only one
569 extensional stage was interpreted (HTM1, **Fig. 7c**).

570 The outcrops located closer to the HPP (HTM 17, 31, 32, **Figs. 5 and 7**) show E-W
571 faults. HTM5 is located on the Ubierna Fault, showing a NW-SE trend, whilst HTM3
572 shows NE-SW strike-slip.

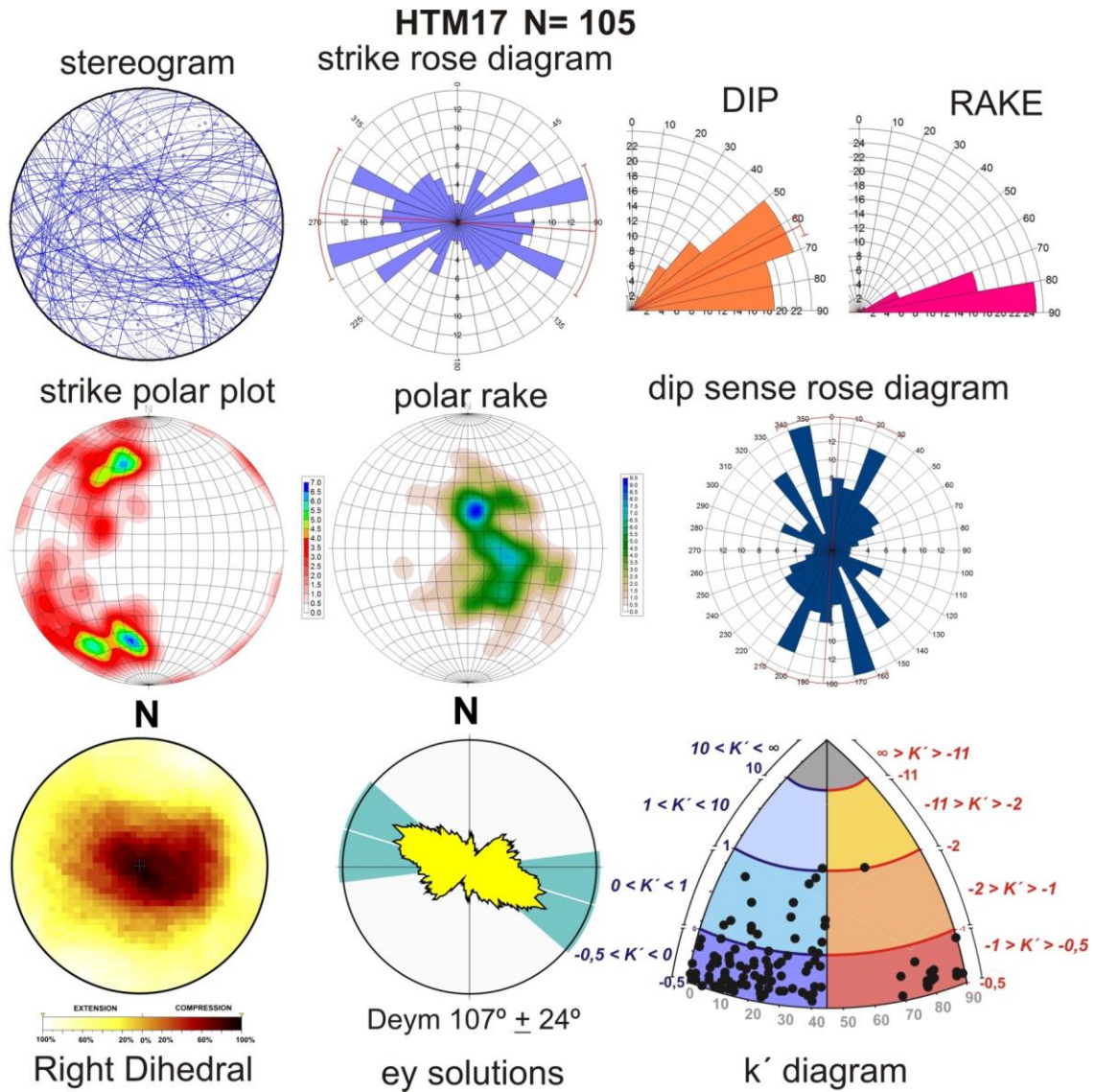
573 Strain analysis suggests that the planes parallel to the S_{Hmax} orientation (NNW-SSE and
574 N-S), could induce the leakage into the reservoir (**Fig. 7**). Moreover, N50°E S_{Hmax}
575 orientation could also affect the reservoir. HPP facilities are close to the Hontomin Fault
576 (**Fig. 5**), a WNW-ESE oriented fault, although the HTM17 station shows that N-S fault
577 planes could play an important role for seepage of fluid into the reservoir.

578

579 **5. DISCUSSION**

580 *5.1 Regional active stress tensor in HTM17 fault pattern*

581



582

583

584 **Figure 8.** Fault data from the outcrop HTM17 located on top of the HPP. See figure 5
 585 for the geographical location. Stereogram plot is lower hemisphere and Schmidt net.

586

587 The active regional field proposed by Herraiz et al. (2000), Stich et al. (2006), Tavani et
 588 al. (2011) and Alcalde et al. (2014), shows e_y , S_{Hmax} with almost NNW-SSE and N-S

589 trends. Namely, the work from Herraiz et al. (2000) calculates three stress tensors

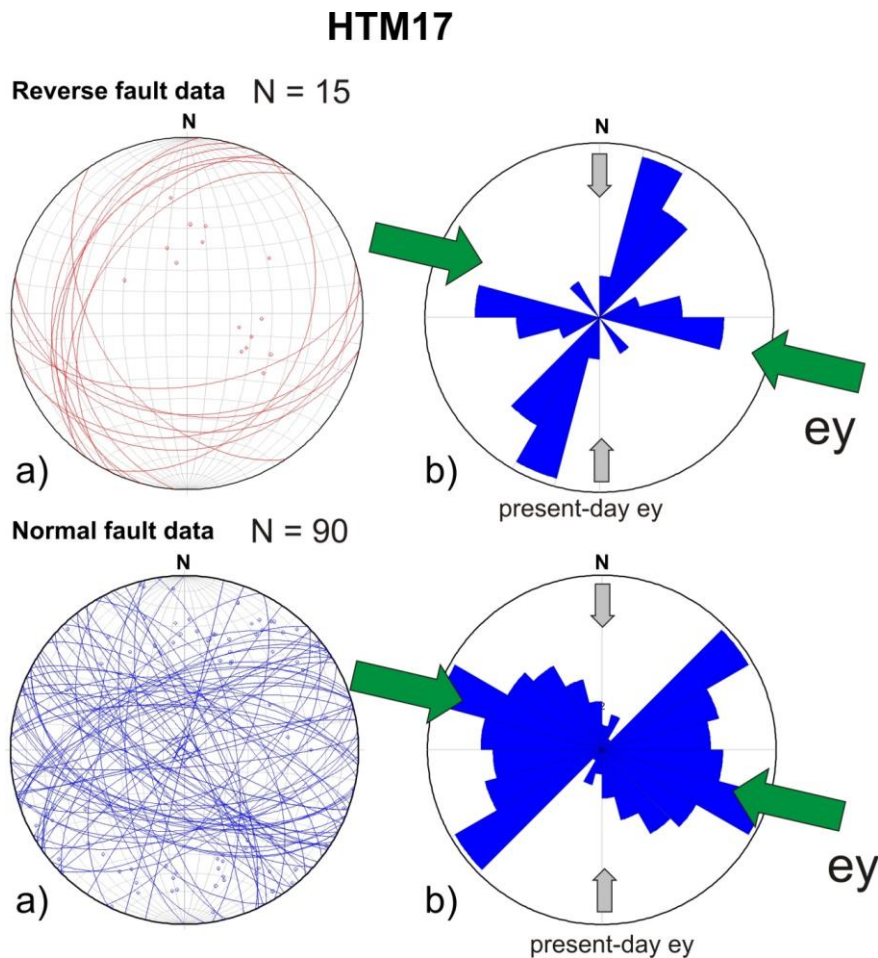
590 within the 20 km of our study area and a Quaternary stress tensor close to the area (c.a.

591 40 km southward of Hontomín). The age of the first one is Miocene, and defined by σ_1

592 $87^\circ/331^\circ$; σ_2 $01^\circ/151^\circ$; σ_3 $00^\circ/061^\circ$ (dip/dip sense 0° - 360°), with an $R=0.06$ and S_{Hmax}

593 trending $N151^\circ E$, under an extensional tectonic regime. Two post-Miocene stress

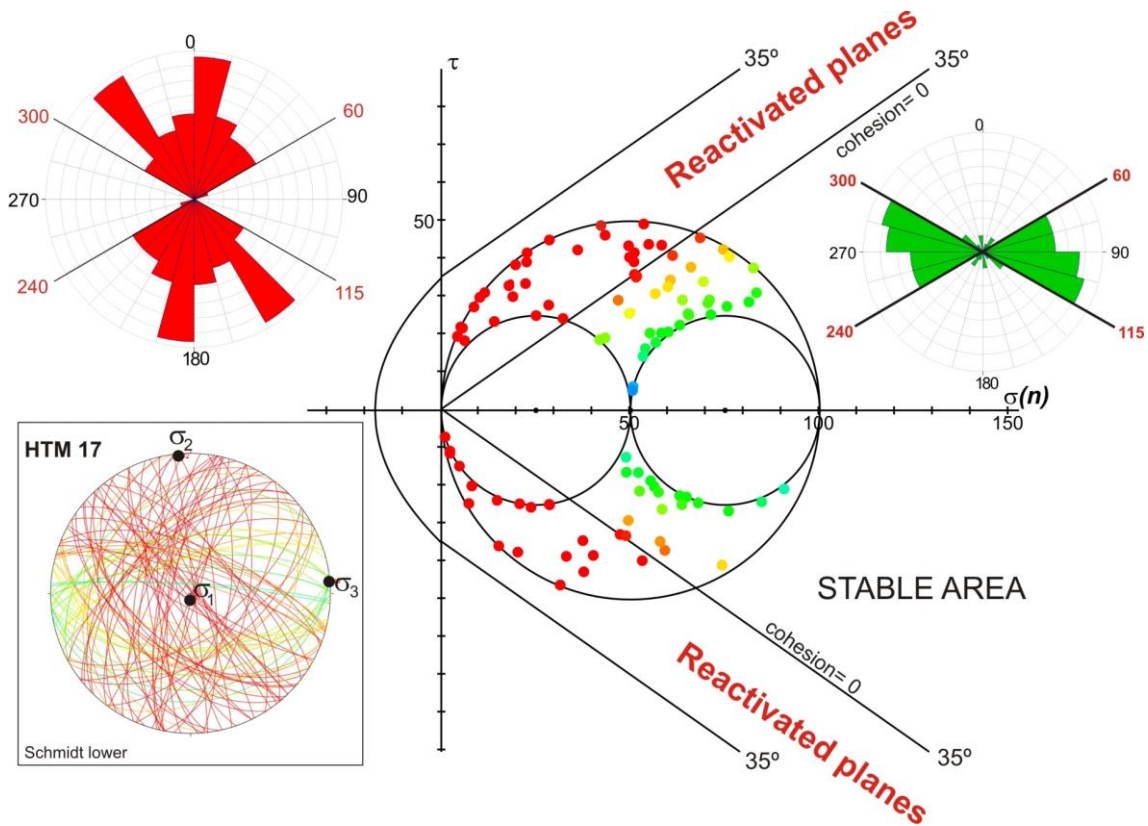
594 tensors are defined by: (1) σ_1 87°/299°; σ_2 00°/209°; σ_3 01°/119° with $R = 0.13$, S_{Hmax}
 595 with N29°E trend under an extensional tectonic regime and (2) σ_1 00°/061°; σ_2
 596 86°/152°; σ_3 03°/331°, with $R=0.76$, and S_{Hmax} N62°E under strike-slip tectonic regime.
 597 Finally, these authors calculated a Quaternary stress tensor defined by: σ_1 85°/183°; σ_2
 598 02°/273°; σ_3 03°/003°; $R=0.02$ and S_{Hmax} with N101°E trend under an extensional
 599 tectonic regime. The regional active stress tensor defined for Pliocene-Quaternary ages
 600 is σ_1 88°/197°; σ_2 01°/355°; σ_3 00°/085° for 327 data with $R = 0.5$ and S_{Hmax} with N-S
 601 trend under an extensional tectonic regional regime.



602
 603 **Figure 9.** Normal and reverse faults stereograms (lower hemisphere and Schmidt net),
 604 and rose diagrams measured in HTM17. Green arrows indicate the orientation of the
 605 local paleostrain field. Grey arrows indicate the orientation of the present-day regional
 606 stress field (Herraiz et al., 2000).

607

608 We have applied the regional active stress tensor (Herraiz et al., 2000) for studying the
 609 reactivation of previous fault patterns measured in HTM17 (Figs. 8 and 9). To carry out
 610 this study, we assume that the fault plane reactivation depends on σ_1 and σ_3 , and the
 611 shape of the failure envelope. Therefore, we have used the Mohr-Coulomb failure
 612 criteria for preexisting fault planes (Xu et al., 2010; Labuz and Zang, 2012), by using
 613 the Mohr Plotter v3.0 code (Allmendinger, 2012). Moreover, to calculate the Mohr-
 614 Coulomb circle, it is necessary to know the cohesion and friction parameters of the
 615 reservoir rock. Bearing in mind that the reservoir rocks are Lower-Jurassic carbonates
 616 (dolostone and oolitic limestone, Alcalde et al., 2013, 2014; Ogaya et al., 2013), we
 617 have assumed the averaged cohesion for carbonates (limestone and dolostone) in 35°
 618 and the coefficient of internal friction of 0.7 (Goodman, 1989). In addition, we have
 619 assumed no cohesion with an angle of static friction of 0.7 for preexisting faults.

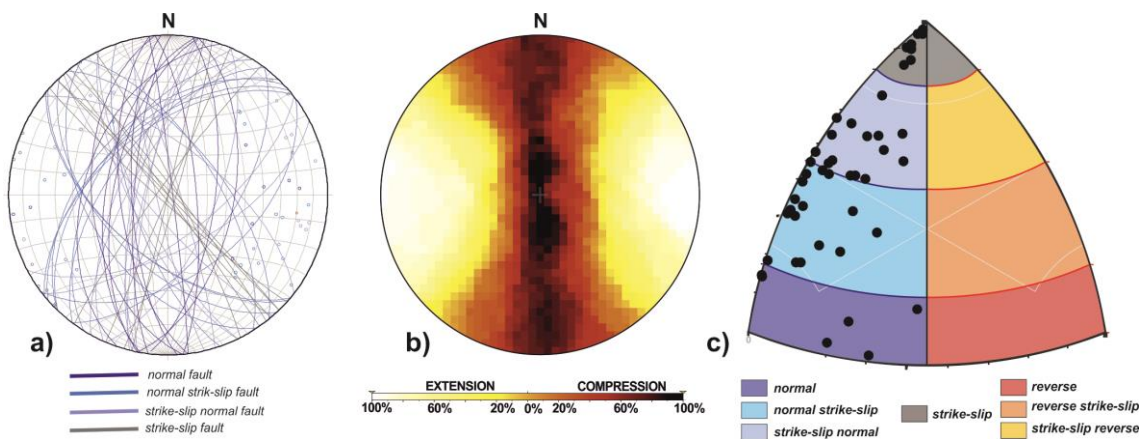


620
 621 **Figure 10.** Mohr-Coulomb failure analysis for the fault-slip data measured in HTM17
 622 under the present-day stress tensor determined by Herraiz et al. (2000). Red dots are
 623 faults reactivated, and green and orange dots are located within the stable zone. Red

624 rose diagram shows the orientation of reactivated faults, between N-S to N60°E and
 625 from N115°E to N180°E. Green rose diagram shows the fault orientation for faults non-
 626 reactivated under the active tress field within the area. See text for further details.

627

628 Figure 10 shows the main results for the Mohr analysis. The reactivated planes under
 629 the active-present stress field are red dots, 52 out of the original 105 fault-slip
 630 measurements at HTM17. Green and orange dots indicate faults with no tectonic
 631 strength accumulation under the present-day stress field. Reactivated fault sets are
 632 oriented between N to N60°E and N115° to 180°E, with N-S and NNE-SSW as main
 633 trends (**Fig. 10**, red rose diagram). Under an extensional tectonic field with $R = 0.5$, N-S
 634 are normal faults, whereas NNE-SSW and NNW-SSE trends are strike-slips faults with
 635 extensional component. According to the results shown in figure 10, these faults could
 636 be reactivated without a pore pressure increase. The inactive fault orientation is
 637 constrained between N60°E and N115°E, mainly WNW-ESE (**Fig. 10**, green rose
 638 diagram). Regarding the uncertainties of these fault orientations, these values can
 639 oscillate $\pm 5^\circ$, according to the field error measurement (averaged error for measuring
 640 structures by a compass).



641

642

643 **Figure 11.** a) Stereogram and poles of fault sets (HTM17) reactivated under the present-
 644 day stress field suggested by Herraiz et al. (2000). b) Right-Dihedral of the reactivated
 645 fault sets. c) K' -strain diagram showing the type of fault for each fault-set.

646 Concerning the reliability of the results, some constrains need to be explained. The
647 Mohr-Coulomb failure criterion is an approximation that assumes that the normal stress
648 on the fault plane is not tensile. Furthermore, the increasing of pore pressure in the
649 reservoir rock reduces the normal stress on the plane of failure and the interval of fault
650 reactivation could be higher. This effect was not considered in the previous analysis
651 since the calculation of the critical pore pressure is beyond the purpose of this work.
652 Nevertheless, the MohrPlotter software ([Allmendinger, 2012](#)), allows estimating the
653 increase of pore pressure to the critical value under some conditions.

654 Finally, we have applied the Slip Model and Right Dihedral to the reactivated fault-slip
655 data from HTM17 outcrop (**Fig. 11**), by including the rake estimated from the active
656 regional stress tensor determined by [Herraiz et al. \(2000\)](#). At a glance, faults oriented
657 between N10°E and N10°W act as normal faults (4 out 52, **Figs. 11a, c**), faults between
658 N10°E - N50°E, and N10°W – N50°W act as extensional faults with strike-slip
659 component (31 out 52), and NE-SW and NW-SE vertical faults act as pure strike slips
660 (8 out 52). The Right Dihedral shows a tectonic regime of strike-slip with extensional
661 component (see [De Vicente et al., 1992](#)), with orthorhombic symmetry and S_{Hmax}
662 oriented N10°W, which is in agreement with the stress-tensor proposed by [Herraiz et al.](#)
663 [\(2000\)](#) with $\sigma_2 = 01^\circ/355^\circ$ and σ_1 vertical. However, strain analysis in this case shows
664 a strike-slip extensional tectonic regime, instead of the extensional regime derived from
665 the stress field. Despite this, both the Mohr-Coulomb analysis and the Paleostain
666 analysis (SM and RD), suggest N-S normal faulting, NNE-SSW to NE-SW and NNW-
667 SSE to NW-SE strike-slips as the active fault network affecting the reservoir. [De](#)
668 [Vicente et al. \(1992\)](#) pointed out that the SM analysis is more robust applied in fault-
669 slip data classified previously by other techniques. Here, we have used the Mohr

670 Coulomb failure criteria to separate active fault set under the same strain tensor,
671 yielding robustness to the results from SM and RD analysis.

672

673 *5.2 Active faulting in the surrounding of HPP*

674 Quaternary tectonic markers for the UFS are suggested by [Tavani et al. \(2011\)](#).

675 According to the tectonic behavior of this fault as right-lateral strike-slip, and the fault

676 segments proposed by [Tavani et al. \(2011\)](#), ranging between 12 and 14 km long, the

677 question is whether this fault could trigger significant earthquakes and which could be

678 the maximum associated magnitude. This is a relevant question given that the “natural

679 seismicity” in the vicinity could affect the integrity of the caprock. Bearing in mind the

680 expectable long-life for the reservoir, estimated in thousands of years, the potential

681 natural earthquake that this master fault could trigger has to be estimated. In this sense,

682 it is necessary to depict seismic scenarios related to large earthquake triggering;

683 however, this type of analysis is beyond the focus of this work.

684 The information that we have to manage in the area of influence (20 km) is: (a)

685 the instrumental seismicity, (b) the geometry of the fault, (c) the total surface rupture,

686 (d) the upper crust thickness and (e) the heat flow across the lithosphere. Starting for the

687 heat flow value, the Hontomín wells show a value that lies between 62 and 78 mW/m²

688 at a 1,500 m depth approximately ([Fernández et al., 1998](#)). Regarding the Moho depth

689 in the area, these aforementioned authors obtained a value ranging between 36 and 40

690 km depth, while the lithosphere base ranges between 120 and 130 km depth ([Torre et](#)

691 [al., 2015](#)). The relevance of this value is the study of the thermal weakness into the

692 lithosphere that could nucleate earthquakes in intraplate areas ([Holford et al., 2011](#)). For

693 these authors, the comparison between the crustal heat-flow in particular zones, in

694 contrast with the background regional value, could explain large seismicity and high

695 rates of small earthquakes occurrence, as the case of the New Madrid seismic zone
696 (Landgraf et al., 2018). For example, in Australia heat-flow values as much as 90
697 mW/m^2 are related with earthquakes sized $M > 5$ (Holford et al., 2011).

698 Regarding the maximum expected earthquake into the zone, we have applied the
699 empirical relationships obtained by Wells and Coppersmith (1994). We have used the
700 equations for strike-slip earthquakes according to the strain field obtained in the area
701 (pure shear), and the surface rupture segment for the Ubierna Fault System, assuming a
702 surface rupture segments between 12 and 14 km (Tavani et al., 2011). The obtained
703 results show that the maximum expected earthquake ranges between M 6.0 and M 6.1.
704 Wells and Coppersmith (1994) indicate for these fault parameters a total area rupture
705 ranging between 140 and 150 km^2 . Surface fault traces rupture as lower as 7 km needs
706 at least 20 km of depth in order to reach a value of the fault-area rupturing greater than
707 100 km^2 , in line with a Moho between 36 and 40 in depth.

708 Regarding the instrumental earthquakes recorded into the area, the two largest
709 earthquakes recorded correspond to magnitude M 3.4 and M 3.3, with a depth ranging
710 between 8 and 11 km, respectively, and a felt macroseismic intensity of III (EMS98,
711 www.ign.es, last access on May, 2019). Both earthquakes occurred between 50 and 60
712 km of distance from the Hontomín Pilot Plant. Only five earthquakes have been
713 recorded within the 20-km radius area of influence and with small magnitudes ranging
714 between M 1.5 and M 2.3. The interesting data is the depth of these earthquakes,
715 ranging between 10 and 20 km, which suggest that the seismogenic crust could reach 20
716 km of depth.

717

718 *5.3 Local tectonic field and induced seismicity*

719 The fluid injection into a deep saline aquifer, which is used as GSC, generally increases
720 the pore pressure. The increasing of the pore pressure migrates from the point of
721 injection to the whole reservoir. Moreover, changes into the stress field for faults that
722 are located below the reservoir, could also trigger induced earthquakes (Verdon et al.,
723 2014). Nevertheless, to understand this possibility and the study the volumetric strain
724 field spatial distribution is required (Lisle et al., 2009).

725 We have applied a physic model to estimate the total volume injected (room
726 conditions), and then we have applied the McGarr's (2014) approximation. The
727 injection of 10 k tons of CO₂ in Hontomín (Gastine et al., 2017), represents an
728 approximated injected volume of CO₂ of 5.56 x10⁶ m³ (room conditions). We have used
729 the expression Mo(max) (Nm) = G ·ΔV (McGarr 2014, eq. 13), where G is the modulus
730 of rigidity and for the upper limit is 3 x 10¹⁰ Pa, and ΔV is the total injected volume (in
731 room conditions). The result is Mo(max) equal to 1.67 x 10¹⁷ Nm (Joules), which
732 corresponds to a maximum seismic moment magnitude Mw (max) = 5.45, by applying
733 the equation Mw = (Log Mo(max) – 9.05)/1.5 from Hanks and Kanamori (1979); where
734 Log is the logarithm to the base 10. McGarr (2014) applied this approach for three
735 cases: (1) wastewater injection, (2) hydraulic fracturing, and (3) geothermal injection.
736 We propose to include this approach for fluid injection related to geological storage of
737 CO₂. We assume that the pore pressure increases from CO₂ injection in a similar way
738 that wastewater does (originally defined by Frohlich, 2012). According to McGarr
739 (2014), the utility of the analysis we have performed is “to predict in advance of a
740 planned injection whether there will be induced seismicity”, and in the case of the HPP,
741 to estimate of the “total injected volume” in a small-scale injection plant. Therefore, the
742 earthquake magnitude to this fluid-injected volume according to the McGarr (2014) and
743 Verdon et al. (2014) could be M > 5 if there are faults with a minimum size of 4 km and

744 oriented according to the present-day stress field (N-S extensional faults and NNE-
745 SSW/NNW-SSE strike slip faults; **Fig. 10**). In the case of HPP, there are faults below
746 the reservoir with this potential earthquake triggering (Alcalde et al., 2014). Also
747 according to McGarr (2014), this value has not to be considered as an absolute physic
748 limit but as a qualitative approximation. Alternatively, increasing by overpressure of the
749 carbonate reservoir along with the pore pressure variations of about 0.5 MPa could
750 trigger earthquakes, as well. Stress-drop related to fluid injections are also reported
751 (Huang et al., 2016).

752 Le Gallo and de Dios (2018) described two main fault sets affecting the reservoir with
753 N-S and E-W trend, respectively. According to the present-day stress tensor described
754 by Herraiz et al. (2000) and Tavani et al. (2011), E-W fault-sets are accommodating
755 horizontal shortening, which means that the permeability could be low. Besides, these
756 faults are decoupled from the present-day stress tensor. However, N-S faults could act
757 as normal faults and, hence, with higher permeability. In this sense, the study of focal
758 mechanisms solutions could improve the safety management, even for
759 microearthquakes of magnitude lesser than M 3.

760 Moreover, the CO₂ lateral diffusion and pressure variation change during the fluid
761 injection phase, and then the system would relax before to be increased during the next
762 injection phase. In this context, the intermittent and episodic injection of CO₂ could also
763 trigger earthquakes by the stress-field and fluid pressure variations in short time periods.

764

765 6. CONCLUSIONS

766 The application of the analysis for brittle deformation determines the tectonic evolution
767 of the strain field, applied in Geological Carbon Storage (GSC). The possibility that
768 pore pressure variations due to fluid injection could change the stress/strain conditions

769 in the reservoir's caprock, makes the study of the present-day tectonic field as
770 mandatory for the storage safety operations. In this sense, we have to bear in mind that
771 this kind of subsurface storage is designed for long-life expectancy, about thousands of
772 years, and therefore, relevant earthquakes could occur affecting the sealing and the
773 seepage of CO₂, compromising the integrity of the reservoir. Hence, we can conclude
774 from our analysis the following items:

775 (1) The study of this tectonic field allows classifying the geometry of the faults to
776 prevent prone earthquake-related structures and design monitoring seismic network.

777 (2) The influence area around the facilities of the GSC for studying the active
778 stress/strain field could reach 20 km from the facility and the tectonic evolution of the
779 geological history of the reservoir have to be established, adding missing information
780 from map scale and boreholes. This information could be used from the 3D local
781 fracture pattern estimation to avoid the pore overpressure. Analysis of the stress-drop
782 due to the fluid injection could be combined with this information to understand
783 potential microseismicity associated with the injection operations.

784 (3) In the case of Hontomín Pilot-Plant, we have obtained two strain active tectonic
785 fields featured as shear deformation. These fields are defined by (a) a local tectonic
786 strain field with e_y , S_{Hmax} striking N50°E and (b) the regional one defined by e_y , S_{Hmax}
787 with N150°E trend. In this context, strike-slip faults with N-S, NNE-SSW and NNW-
788 SSE trends, are accumulating present-day tectonic deformation. Analysis of Mohr-
789 Coulomb failure criterion shows a potential reactivation of these fault sets.

790 (4) N-S faults are accumulating tectonic deformation and they could act as normal
791 faults. This means that this fault set is the preferential direction for potential fluid
792 leakage. In addition, intersection with NNE-SSW and NNW-SSE could arrange 3D
793 networks for fluid mobilization and leakage.

794 (5) The Ubierna Fault System represents a tectonically active fault array that could
795 trigger natural earthquakes as large as M 6 (± 0.1), from the empirical relationship of the
796 total rupture segment (ranging between 12 and 14 km, and the total fault-area rupture,
797 oscillating between 100 and 150 km²). Despite the lack of instrumental seismicity into
798 the influence area, we cannot obviate the potential earthquake occurrence within
799 intraplate areas due to the long- timescale expected-life of the GSC. The heat-flow
800 values and thermal crust conditions could determine the presence of intraplate
801 earthquakes with magnitude $M > 5$, for a long timescale (thousands of years).

802 The tectonic evolution and kinematics of the west part of the Burgalesa Platform
803 domain from upper Triassic to present day show a Cretaceous tectonic inversion, local
804 reverse strain field during the early Oligocene and early Miocene, with a Normal strain
805 field during the middle Miocene. The active strain field is now defined by an
806 extensional tectonic defined by e_y with N-S trend, activating N-S normal faults and
807 right-lateral faults with NNW- and NNE- trends.

808 Finally, we state that the determination of the active tectonic strain field, the recognition
809 and study of active faults within the area of influence (20 km), the estimation of the
810 maximum potential triggered natural earthquake, the modeling of the stress-change
811 during the fluid injection and stress-drop, probably improve the operations for a secure
812 storage. In a short future, earthquake scenarios will be the next step: modeling the
813 Coulomb static stress-changes due to fluid injection and the modeling of intensity maps
814 of horizontal seismic acceleration.

815

816 ACKNOWLEDGEMENTS

817 Thanks are given to Pr. Graham Yielding and an anonymous reviewer for their remarks
818 during the open discussion. We wish to thank Pr. Allmendinger for the free use of the
819 MohrPlotter 3.0 software, last access in March of 2020 at the web browser:
820 <http://www.geo.cornell.edu/geology/faculty/RWA/programs/mohrplotter.html>. This
821 work has been partially supported by the European Project ENOS: ENabling Onshore
822 CO₂ Storage in Europe, H2020 Project ID: 653718 and the Spanish project 3GEO,
823 CGL2017-83931-C3-2-P, MICIU-FEDER. The authors would also thank the crew of
824 CIUDEN at Hontomín facilities for their kind assistance during our fieldwork.

825

826 REFERENCES

- 827 Alcalde, J., Martí, D., Calahorrano, A., Marzan, I., Ayarza, P., Carbonell, R., Juhlin, C.,
828 and Pérez-Estaún, A.: Active seismic characterization experiments of the Hontomín
829 research facility for geological storage of CO₂, Spain, *Int. J. Greenh. Gas Con.*, 19,
830 785–795, <http://dx.doi.org/10.1016/j.ijggc.2013.01.039>, 2013.
- 831 Alcalde J., Marzán I., Saura E., Martí D., Ayarza P., Juhlin C., Pérez-Estaún, A., and
832 Carbonell, R.: 3D geological characterization of the Hontomín CO₂ storage site,
833 Spain: Multidisciplinary approach from seismic, well-log and regional data,
834 *Tectonophysics*, 627, 6–25, <http://dx.doi.org/10.1016/j.tecto.2014.04.025>, 2014.
- 835 Allmendinger, R. W., Cardozo, N. C., and Fisher, D.: *Structural Geology Algorithms:
836 Vectors & Tensors*, Cambridge, England, Cambridge University Press, 289 pp, 2012.
- 837 Álvarez-Gómez, J. A.: FMC: a one-liner python program to manage, classify and plot
838 focal mechanisms, EGU General Assembly, Vienna, Austria, 27 April-02 May,
839 EGU2014-10887, 2014.
- 840 Anderson, E. M.: *The Dynamics of Faulting and Dyke Formation with application to
841 Britain*, 2nd ed., Oliver and Boyd, Edinburgh, 206 pp., 1951.
- 842 Angelier, J.: Determination of the mean principal directions of stresses for a given fault
843 population, *Tectonophysics*, 56, 17-26, [https://doi.org/10.1016/0040-1951\(79\)90081-](https://doi.org/10.1016/0040-1951(79)90081-7)
844 [7](https://doi.org/10.1016/0040-1951(79)90081-7), 1979.
- 845 Angelier, J.: Tectonic analysis of fault slip data sets, *J. Geophys. Res.*, 89, 5835-5848,
846 <https://doi.org/10.1029/JB089iB07p05835>, 1984.
- 847 Angelier, J.: Inversion of field data in fault tectonics to obtain the regional stress-III. A
848 new rapid direct inversion method by analytical means, *Geophys. J. Int.*, 103, 363-
849 376, <https://doi.org/10.1111/j.1365-246X.1990.tb01777.x>, 1990.
- 850 Angelier, J. and Mechler, P.: Sur une méthode graphique de recherche des contraintes
851 principales également utilisable en tectonique et en séismologie: la méthode des
852 dièdres droits, *B. Soc. Geol. Fr.*, 19, 1309-1318,
853 <http://dx.doi.org/10.2113/gssgfbull.S7-XIX.6.1309>, 1977.
- 854 Aurell, M., Meléndez, G., Olóriz, F., Bádenas, B., Caracuel, J. E., García-Ramos, J. C.,
855 Goy, A., Linares, A., Quesada, S. and Robles, S.: Jurassic, in *The geology of Spain*,
856 pp. 213–253, The Geological Society of London., 2002.
- 857 Bentham, M. and Kirby, G.: CO₂ Storage in Saline Aquifers. *Oil Gas Sci. Technol.*, 60,
858 559-567, <https://doi.org/10.2516/ogst:2005038>, 2005.

- 859 Bott, M.H.P.: The mechanism of oblique-slip faulting, *Geol. Mag.*, 96: 109-117.
860 <https://doi.org/10.1017/S0016756800059987>, 1959.
- 861 Capote, R., De Vicente, G., and González Casado, J. M.: An application of the slip
862 model of brittle deformation to focal mechanism analysis in three different plate
863 tectonics situation. *Tectonophysics*, 191, 399-409, [https://doi.org/10.1016/0040-](https://doi.org/10.1016/0040-1951(91)90070-9)
864 [1951\(91\)90070-9](https://doi.org/10.1016/0040-1951(91)90070-9), 1991.
- 865 Calvet, F., Anglada, E. and Salvany, J. M.: El Triásico de los Pirineos, in Vera, J.A.
866 (ed.) *Geología de España*, pp. 272–274, SGE–IGME, Madrid, 2004.
- 867 Carola, E.: The transition between thin-to-thick-skinned styles of deformation in the
868 Western Pyrenean Belt. Ph. D. thesis, Universitat de Barcelona, 271 pp., 2004.
- 869 Christensen, N. P.: Report on the current state and need for further research on CO₂
870 capture and storage. CO2NET, European Carbon Dioxide Network,
871 www.co2net.com, 2004.
- 872 Chu, S.: Carbon Capture and Sequestration, *Science*, 325, 1599,
873 <http://dx.doi.org/10.1126/science.1181637>, 2009.
- 874 Dallmeyer, R. D. and Martínez-García, E., Eds.: *Pre-Mesozoic Geology of Iberia*,
875 Springer-Verlag, Berlin Heidelberg, 1990.
- 876 De Vicente, G.: Análisis Poblacional de Fallas. El sector de enlace Sistema Central-
877 Cordillera Ibérica. Ph. D. thesis, Universidad Complutense de Madrid, Spain, 317
878 pp., 1988.
- 879 De Vicente, G. Muñoz, A., Giner, J.L.: Use of the Right Dihedral Method: implications
880 from the Slip Model of Fault Population Analysis, *Rev. Soc. Geol. España*, 5(3-4), 7-
881 19. 1992.
- 882 De Vicente, G., Cloetingh, S., Muñoz-Martín, A., Olaiz, A., Stich, D., Vegas, R.,
883 Galindo-Zaldívar, J., and Fernández-Lozano, J.: Inversion of moment tensor focal
884 mechanisms for active stresses around Microcontinent Iberia: Tectonic implications,
885 *Tectonics*, 27: 1-22, <http://dx.doi.org/10.1029/2006TC002093>, 2008.
- 886 De Vicente, G., Cloetingh, S., Van Wees, J. D., and Cunha, P. P.: Tectonic
887 classification of Cenozoic Iberian foreland basins, *Tectonophysics*, 502, 38–61,
888 <http://dx.doi.org/10.1016/j.tecto.2011.02.007>, 2011.
- 889 Etchecopar, A., Vasseur, G., and Daignieres, M.: An inverse problem in microtectonics
890 for the determination of stress tensor from fault striation analysis, *J. Struct. Geol.*, 3,
891 51-65, [http://dx.doi.org/10.1016/0191-8141\(81\)90056-0](http://dx.doi.org/10.1016/0191-8141(81)90056-0), 1981.

- 892 Fernández, M., Marzán, I., Correia, A., and Ramalho, E.: Heat flow, heat production,
893 and lithospheric thermal regime in the Iberian Peninsula, *Tectonophysics*, 291, 29-
894 53, [http://dx.doi.org/10.1016/S0040-1951\(98\)00029-8](http://dx.doi.org/10.1016/S0040-1951(98)00029-8), 1998.
- 895 Foulger, G. R., Wilson, M., Gluyas, J., Julian, B. R. and Davies, R.: Global review of
896 human-induced earthquakes, *Earth-Sci. Rev.*, 178, 438–514,
897 <http://dx.doi.org/10.1016/j.earscirev.2017.07.008>, 2018.
- 898 Frohlich, C.: Two-year survey comparing earthquake activity and injection-well
899 locations in the Barnett Shale, Texas. *PNAS*, vol. 109 (35), 13934 – 13938,
900 <https://doi.org/10.1073/pnas.1207728109>, 2012.
- 901 García-Mondéjar, J., Pujalte, V. and Robles, S.: Características sedimentológicas,
902 secuenciales y tectoestratigráficas del Triásico de Cantabria y norte de Palencia,
903 *Cuad. Geol. Ibérica*, (10), 151–172, 1986.
- 904 García-Mondéjar, J., Agirrezabala, L. M., Aranburu, A., Fernández-Mendiola, P. A.,
905 Gómez-Pérez, I., López-Horgue, M. and Rosales, I.: Aptian-Albian tectonic pattern
906 of the Basque-Cantabrian Basin (Northern Spain), *Geological Journal*, 31(1), 13–45,
907 [http://dx.doi.org/10.1002/\(SICI\)1099-1034\(199603\)31:1<13::AID-GJ689>3.0.CO;2-](http://dx.doi.org/10.1002/(SICI)1099-1034(199603)31:1<13::AID-GJ689>3.0.CO;2-Y)
908 [Y](http://dx.doi.org/10.1002/(SICI)1099-1034(199603)31:1<13::AID-GJ689>3.0.CO;2-Y), 1996.
- 909 Gastine, M., Berenblyum, R., Czernichowski-lauriol, I., de Dios, J. C., Audigane, P.,
910 Hladik, V., Poulsen, N., Vercelli, S., Vincent, C., and Wildenborg, T.: Enabling
911 onshore CO₂ storage in Europe: fostering international cooperation around pilot and
912 test sites, *Energy Proced.*, 114, 5905–5915,
913 <http://dx.doi.org/10.1016/j.egypro.2017.03.1728>, 2017.
- 914 Giner-Robles, J.L., Pérez-López, R., Elez, J., Silva, P.G., Rodríguez Escudero, E.,
915 Canora, C., Rodríguez-Pascua, M.A., Bardají, T., Roquero, E., Huerta, P., Perucha,
916 M.A.: Strain analysis in the Iberian Peninsula from focal mechanism solutions,
917 seismic hazard impacts, In: C. Canora, F. Martín, E. Masana, R. Pérez y M. Ortuño,
918 Eds., pp. 249-252. Tercera reunión ibérica sobre fallas activas y paleosismología,
919 Alicante (España), 2018.
- 920 Goldberg, D. S., Kent, D. V., and Olsen, P. E.: Potential on-shore and off-shore
921 reservoirs for CO₂ sequestration in Central Atlantic magmatic province basalts, P.
922 *Natl. Acad. Sci. USA*, 107, 1327–1332, <http://dx.doi.org/10.1073/pnas.0913721107>,
923 2010.

- 924 Gómez, M., Vergés, J. and Riaza, C.: Inversion tectonics of the northern margin of the
925 Basque Cantabrian Basin, *Bulletin de la Société Géologique de France*, 173(5), 449–
926 459, <http://dx.doi.org/10.2113/173.5.449>, 2002.
- 927 Goodman, R. E.: *Introduction to Rock Mechanics*, 2nd Edition, John Wiley & Sons, Inc.,
928 New York. 576 pp., 1989.
- 929 Hanks, T.C., Kanamori, H.: A Moment Magnitude Scale, *J. Geophys. Res.*, 84 (B5),
930 2348–2350, <https://doi.org/10.1029/JB084iB05p02348>, 1979.
- 931 Herraiz, M., De Vicente, G., Lindo-Naupari, R., Giner, J., Simón, J.L., González-
932 Casado, J.M., Vadillo, O., Rodríguez-Pascua, M.A., Cicuéndez, J.I., Casas, A.,
933 Cabañas, L., Rincón, P., Cortés, A.L., Ramírez, M., and Lucini, M.: The recent
934 (upper Miocene to Quaternary) and present tectonic stress distributions in the Iberian
935 Peninsula, *Tectonics*, 19, 762–786, <https://doi.org/10.1029/2000TC900006>, 2000.
- 936 Holford, S. M., Hillis, R. R., Hand, M., and Sandiford, M.: Thermal weakening
937 localizes intraplate deformation along the southern Australian continental margin,
938 *Earth Planet. Sc. Lett.*, 305, 207–214, <http://dx.doi.org/10.1016/j.epsl.2011.02.056>,
939 2011.
- 940 Huang, Y., Beroza, G. C., and Ellsworth, W. L.: Stress drop estimates of potentially
941 induced earthquakes in the Guy-Greenbrier sequence, *J. Geophys. Res.-Sol. Ea.*, 121,
942 6597–6607, <http://dx.doi.org/10.1002/2016JB013067>, 2016.
- 943 Kaverina, A. N., Lander, A. V., and Prozorov, A. G.: Global creepex distribution and its
944 relation to earthquake-source geometry and tectonic origin, *Geophys. J. Int.*, 125,
945 249-265, <https://doi.org/10.1111/j.1365-246X.1996.tb06549.x>, 1996.
- 946 Labuz, J. F., Zang, A.: Mohr–Coulomb Failure Criterion. *Rock Mech. Rock Eng.*, 45,
947 975–979, <https://doi.org/10.1007/s00603-012-0281-7>, 2012.
- 948 Landgraf, A., Kuebler, S., Hintersberger, E., Stein, S.: Active tectonics, earthquakes and
949 palaeoseismicity in slowly deforming continents, Landgraf, A., Kuebler, S.,
950 Hintersberger, E. & Stein, S. (eds) *Seismicity, Fault Rupture and Earthquake
951 Hazards in Slowly Deforming Regions*. Geological Society, London, Special
952 Publications, 432, <http://doi.org/10.1144/SP432.13>, 2018.
- 953 Le Gallo, Y. and de Dios, J. C.: Geological Model of a Storage Complex for a CO₂
954 Storage Operation in a Naturally-Fractured Carbonate Formation, *Geosciences*, 2018,
955 8, 354, <http://dx.doi.org/10.3390/geosciences8090354>, 2018.

- 956 Le Pichon, X. and Sibuet, J.-C.: Western extension of boundary between European and
957 Iberian plates during the Pyrenean orogeny, *Earth and Planetary Science Letters*,
958 12(1), 83–88, [http://dx.doi.org/10.1016/0012-821X\(71\)90058-6](http://dx.doi.org/10.1016/0012-821X(71)90058-6), 1971.
- 959 Lepvrier, C. and Martínez-García, E.: Fault development and stress evolution of the
960 post-Hercynian Asturian Basin (Asturias and Cantabria, northwestern Spain),
961 *Tectonophysics*, 184, 345, [http://dx.doi.org/10.1016/0040-1951\(90\)90447-G](http://dx.doi.org/10.1016/0040-1951(90)90447-G), 1990.
- 962 Lisle, R. J., Aller, J., Bastida, F., Bobillo-Ares, N. C., and Toimil, N. C.: Volumetric
963 strains in neutral surface folding, *Terra Nova*, 21, 14–20,
964 <http://dx.doi.org/10.1111/j.1365-3121.2008.00846.x>, 2009.
- 965 McGarr, A.: Maximum magnitude earthquakes induced by fluid injection, *J. Geophys.*
966 *Res.*, 119, 1008–1019, <https://doi.org/10.1002/2013JB010597>, 2014.
- 967 McNamara, D.D. Methods and techniques employed to monitor induced seismicity
968 from carbon capture and storage, *GNS Science Report 2015/18*, 23 pp.,
969 <http://dx.doi.org/10.13140/RG.2.2.13830.98888>, 2016.
- 970 Muñoz, J. A.: Evolution of a continental collision belt: ECORS-Pyrenees crustal
971 balanced cross-section, in *Thrust Tectonics*, edited by K. R. McClay, pp. 235–246,
972 Springer Netherlands, Dordrecht., 1992.
- 973 Ogaya, X., Ledo J., Queralt P., Marcuello, A., and Quintà, A.: First geoelectrical image
974 of the subsurface of the Hontomín site (Spain) for CO₂ geological storage: A
975 magnetotelluric 2D characterization, *Int. J. Greenh. Gas Con.*, 13, 168–179,
976 <https://dx.doi.org/10.1016/j.ijggc.2012.12.023>, 2013.
- 977 Orr, F.M.: Onshore Geologic Storage of CO₂, *Science*, 325, 1656-1658,
978 <http://dx.doi.org/10.1126/science.1175677>, 2009.
- 979 Pan, P., Wu, Z., Feng, X., Yan, F.: Geomechanical modeling of CO₂ geological storage:
980 A review, *J. Rock Mech. and Geotech. Eng.*, 8, 936-947,
981 <http://dx.doi.org/10.1016/j.jrmge.2016.10.002>, 2016.
- 982 Pérez-López, R., Mediato, J.F., Rodríguez-Pascua, M.A., Giner-Robles, J.L., Martínez-
983 Orío, R., Arenillas-González, A., Fernández-Canteli, P., de Dios, J.C., Loubeau, L.:
984 Aplicación del análisis estructural y campos de deformación para el estudio de
985 sismicidad inducida en almacenamiento profundo: Hontomín, In: C. Canora, F.
986 Martín, E. Masana, R. Pérez y M. Ortuño, Eds., pp. 279-282. Tercera reunión ibérica
987 sobre fallas activas y paleosismología, Alicante (España), 2018.
- 988 Pearce, J. M.: What can we learn from Natural Analogues? An overview of how
989 analogues can benefit the geological storage of CO₂, in: *Advances in the Geological*

- 990 Storage of Carbon Dioxide, edited by: Lombardi, S., Altunina, L. K., and Beaubien,
991 S. E., Springer, Dordrecht, The Netherlands, 129–139, 2005.
- 992 Pegoraro, O.: Application de la microtectonique à un étude de neotectonique. Le golfe
993 Maliaque (Grèce centrale). Ph.D. thesis, U.S.T.L. Montpellier, France, 41 pp., 1972.
- 994 Permentier, K., Vercammen, S., Soetaert, S., and Schellemans, Ch.: Carbon dioxide
995 poisoning: a literature review of an often forgotten cause of intoxication in the
996 emergency department, *International Journal of Emergency Medicine*, 10, 14,
997 <http://dx.doi.org/10.1186/s12245-017-0142-y>, 2017.
- 998 Quintà, A. and Tavani S., The foreland deformation in the south-western Basque–
999 Cantabrian Belt (Spain), *Tectonophysics*, 576–577, 4–19,
1000 <http://dx.doi.org/10.1016/j.tecto.2012.02.015>, 2012.
- 1001 Reches, Z.: Faulting of rocks in three-dimensional strain fields, II. Theoretical analysis,
1002 *Tectonophysics*, 95, 133-156, [https://doi.org/10.1016/0040-1951\(83\)90264-0](https://doi.org/10.1016/0040-1951(83)90264-0), 1983.
- 1003 Reches, Z.: Determination of the tectonic stress tensor from slip along faults that obey
1004 the Coulomb yield condition, *Tectonics*, 7, 849-861,
1005 <https://doi.org/10.1029/TC006i006p00849>, 1987.
- 1006 Rice, S. A.: Health effects of acute and prolonged CO₂ exposure in normal and sensitive
1007 populations, Second Annual Conference on Carbon Sequestration, Alexandria,
1008 Virginia, USA, 5-6 May, 2003.
- 1009 Roca, E., Muñoz, J. A., Ferrer, O. and Ellouz, N.: The role of the Bay of Biscay
1010 Mesozoic extensional structure in the configuration of the Pyrenean orogen:
1011 Constraints from the MARCONI deep seismic reflection survey, *Tectonics*, 30(2),
1012 <https://10.1029/2010TC002735>, 2011.
- 1013 Röhmann, L., Tillner, E., Magri, F., Kühn, M., and Kempka, T.: Fault reactivation and
1014 ground surface uplift assessment at a prospective German CO₂ storage site, *Energy*
1015 *Proced.*, 40, 437–446. <http://dx.doi.org/10.1016/j.egypro.2013.08.050>, 2013.
- 1016 Scholz, C.: The seismic cycle. In *The Mechanics of Earthquakes and Faulting* 3rd
1017 edition, Cambridge, Cambridge University Press, pp. 228-277, 2018.
- 1018 Serrano, A. and Martínez del Olmo, W.: Tectónica salina en el Dominio Cantabro–
1019 Navarro: evolución, edad y origen de las estructuras salinas, in: *Formaciones*
1020 *evaporíticas de la Cuenca del Ebro y cadenas perifericas, y de la zona de Levante*,
1021 edited by: Orti, F. and Salvany, J.M., Empresa Nacional De Residuos Radiactivos
1022 S.A, ENRESA-GPPG, Barcelona, Spain, 39–53, 1990.

- 1023 Simpson, R. S.: Quantifying Anderson's fault types, *J. Geophys. Res.*, 102, 17,909-
1024 17,919, <https://doi.org/10.1029/97JB01274>, 1997.
- 1025 Stich, D., Serpelloni, E., Mancilla, F. L., and Morales, J.: Kinematics of the Iberia-
1026 Maghreb plate contact from seismic moment tensors and GPS observations,
1027 *Tectonophysics*, 426, 295-317. <https://doi.org/10.1016/j.tecto.2006.08.004>, 2006.
- 1028 Soto R., Casa-Sainz A. M., and Villalaín, J. J.: Widespread Cretaceous inversion event
1029 in northern Spain: evidence from subsurface and palaeomagnetic data, *Journal of the*
1030 *Geological Society London*, 168, 899-912, [http://dx.doi.org/10.1144/0016-](http://dx.doi.org/10.1144/0016-76492010-072)
1031 [76492010-072](http://dx.doi.org/10.1144/0016-76492010-072), 2011.
- 1032 Tavani, S., Quintá, A., and Granado, P.: Cenozoic right-lateral wrench tectonics in the
1033 Western Pyrenees (Spain): The Ubierna Fault System, *Tectonophysics*, 509, 238-
1034 253, <http://dx.doi.org/10.1016/j.tecto.2011.06.013>, 2011.
- 1035 Tavani, S.: Plate kinematics in the Cantabrian domain of the Pyrenean orogeny, *Solid*
1036 *Earth*, 3, 265–292, <http://dx.doi.org/10.5194/se-3-265-2012>, 2012
- 1037 Tavani, S., Carola, C., Granado, P., Quintà, A., and Muñoz, J. A.: Transpressive
1038 inversion of a Mesozoic extensional forced fold system with an intermediate
1039 décollement level in the Basque - Cantabrian Basin (Spain), *Tectonics*, 32,
1040 <http://dx.doi.org/10.1002/tect.20019>, 2013.
- 1041 Torne, M., Fernández, M., Vergés, J., Ayala, C., Salas, M. C., Jimenez-Munt, I.,
1042 Buffett, G. G., and Díaz, J.: Crust and mantle lithospheric structure of the Iberian
1043 Peninsula deduced from potential field modeling and thermal analysis,
1044 *Tectonophysics*, 663, 419–433, <http://dx.doi.org/10.1016/j.tecto.2015.06.003>, 2015.
- 1045 Tugend, J., Manatschal, G., Kusznir, N. J., Masini, E., Mohn, G. and Thion, I.:
1046 Formation and deformation of hyperextended rift systems: Insights from rift domain
1047 mapping in the Bay of Biscay-Pyrenees, *Tectonics*, 33(7), 1239–1276,
1048 <http://dx.doi.org/10.1002/2014TC003529>, 2014.
- 1049 Vegas, R., Vázquez, J. T., Olaiz, A. J., and Medialdea, T.: Tectonic model for the latest
1050 Triassic - Early Jurassic extensional event in and around the Iberian Peninsula,
1051 *Geogaceta*, 60, 23-26, 2016.
- 1052 Verdon, J. P.: Significance for secure CO₂ storage of earthquakes induced by fluid
1053 injection, *Environ. Res. Lett.*, 9, 064022 (10pp), [http://dx.doi.org/10.1088/1748-](http://dx.doi.org/10.1088/1748-9326/9/6/064022)
1054 [9326/9/6/064022](http://dx.doi.org/10.1088/1748-9326/9/6/064022), 2014.

- 1055 Verdon, J. P., Stork, A. L., Bissell, R. C., Bond, C. E., and Werner, M. J.: Simulation of
1056 seismic events induced by CO₂ injection at In Salah, Algeria, *Earth Planet. Sci. Lett.*,
1057 426, 118–129, <http://dx.doi.org/10.1016/j.epsl.2015.06.029>, 2015.
- 1058 Vergés, J., Fernández, M. and Martínez, A.: The Pyrenean orogen: pre-, syn-, and post-
1059 collisional evolution, *J. Virt. Ex*, 08, <http://dx.doi.org/10.3809/jvirtex.2002.00058>,
1060 2002.
- 1061 Wells, D. L. and Coppersmith, K. J.: New empirical relationships among magnitude,
1062 rupture length, rupture width, rupture area, and surface displacement, *B. Seismol.*
1063 *Soc. Am.*, 84, 974–1002, 1994.
- 1064 Wilson, M. P., Foulger, G. R., Gluyas, J. G., Davies, R. J., and Julian, B. R.: HiQuake
1065 the human-induced earthquake database, *Seismol. Res. Lett.*, 88, 1560-1565,
1066 <http://dx.doi.org/10.1785/0220170112>, 2017.
- 1067 Winthagen, P., Arts, R., and Schroot, B.: Monitoring Subsurface CO₂ Storage. *Oil Gas*
1068 *Sci. Technol.*, 60, 573-582, 2005.
- 1069 Xu, S.-S., A.F. Nieto-Samaniego, S.A. Alaniz-Álvarez: 3D Mohr diagram to explain
1070 reactivation of pre-existing planes due to changes in applied stresses, *Rock Stress*
1071 *and Earthquakes – Xie (ed.)*, 739-745 p, 2010.
- 1072 Žalohar, J. and Vrabec, M.: Combined kinematic and paleostress analysis of fault-slip
1073 data: The Multiple-slip method, *J. Struct. Geol.*, 30, 1603–1613,
1074 <http://dx.doi.org/10.1016/j.jsg.2008.09.004>, 2008.